The Pingding segment of the Altyn Tagh Fault (91°E): Holocene slip-rate determination from cosmogenic radionuclide dating of offset fluvial terraces

A.-S. Mériaux,[1] J. Van der Woerd,[2] P. Tapponnier,[3,4] F. J. Ryerson,[5] R. C. Finkel,[6] C. Lasserre,[7] and X. Xu[8]

Received 6 March 2012; revised 1 August 2012; accepted 10 August 2012; published 25 September 2012.

[1] Morphochronologic slip-rates on the Altyn Tagh Fault (ATF) along the southern front of the Pingding Shan at ~90.5°E are determined by cosmogenic radionuclide (CRN) dating of seven offset terraces at two sites. The terraces are defined based upon morphology, elevation and dating, together with fieldwork and high-resolution satellite analysis. The majority of the CRN model ages fall within narrow ranges (<2 ka) on the four main terraces (T1, T2, T3 and T3′), and allow a detailed terrace chronology. Bounds on the terrace ages and offsets of 5 independent terraces yield consistent slip-rate estimates. The long-term slip-rate of 13.9 ± 1.1 mm/yr is defined at the 95% confidence level, as the joint rate probability distribution of the rate derived from each independent terrace. It falls within the bounds of all the rates defined on the central Altyn Tagh Fault between the Cherchen He (86.4°E) and Akato Tagh (~88°E) sites. This rate is ~10 mm/yr less than the upper rate determined near Tura at ~87°E, in keeping with the inference of an eastward decreasing rate due to progressive loss of slip to thrusts branching off the fault southwards but it is greater than the 9 ± 4 mm/yr rate determined at ~90°E by GPS surveys and other geodetic short-term rates defined elsewhere along the ATF. Whether such disparate rates will ultimately be reconciled by a better understanding of fault mechanics, resolved transient deformations during the seismic cycle or by more accurate measurements made with either approach remains an important issue.

Citation: Mériaux, A.-S., J. Van der Woerd, P. Tapponnier, F. J. Ryerson, R. C. Finkel, C. Lasserre, and X. Xu (2012), The Pingding segment of the Altyn Tagh Fault (91°E): Holocene slip-rate determination from cosmogenic radionuclide dating of offset fluvial terraces, *J. Geophys. Res.*, *117*, B09406, doi:10.1029/2012JB009289.

1. Introduction

[2] Given its great length (~1800 km between 78°E and 97°E) and topographic prominence as a limit between the Tibetan highlands (3000–5000 m a.s.l.) and the Tarim basin (~1000 m a.s.l.), the Altyn Tagh Fault (ATF) is usually considered to be the largest active strike-slip fault of Eurasia. Slip-rate and seismic behavior of the fault are keys to the present-day kinematics of collision tectonics in Asia, and viewed as an important factor in evaluating whether continental deformation can be approximated by block tectonics or not, a topic that remains the subject of debate [*Avouac et al.*, 1993; *Calais et al.*, 2006; *Dayem et al.*, 2009; *England and Houseman*, 1986; *England and Molnar*, 1997; *Hilley et al.*, 2009; *Holt et al.*, 2000; *Loveless and Meade*, 2011; *Meade*, 2007; *Peltzer and Saucier*, 1996; *Thatcher*, 2007; *Vergnolle et al.*, 2007]. Recent slip-rate estimates based on complementary and/or similar techniques currently yield disparate results along the Altyn Tagh Fault. Near Tura (~86.4°E) radiocarbon and CRN dating of offset features at two sites - Cherchen He and Sulamu Tagh - yields left-lateral slip rate of 27 ± 7 mm/yr [*Mériaux et al.*, 2004]. Reinterpretation of the Cherchen He site by *Cowgill* [2007] yield a rate of 9.4 ± 2.3 mm/y. Recently, studies by *Gold et al.* [2009, 2011] on the same Cherchen fault segment yield estimates from 7 to 17 mm/yr for the late Holocene at Kelutelage (86.67°E) and Tuzidun (86.72°E). About 100 km further East at Yukuang (87.87°E), Keke Qiapu (88.12°E) and Yuemake (88.51°E),

[1]School of Geography, Politics and Sociology, Newcastle University, Newcastle upon Tyne, UK.
[2]IPGS-EOST, UMR 7516, CNRS, Université de Strasbourg, Strasbourg, France.
[3]EOS, Nanyang Technological University, Singapore.
[4]Institut de Physique du Globe de Paris, UMR 7154, CNRS, Paris, France.
[5]Lawrence Livermore National Laboratory, Livermore, California, USA.
[6]Earth and Planetary Science Department, University of California, Berkeley, California, USA.
[7]Maison des Géosciences, ISTerre, Grenoble, France.
[8]Central Earthquake Administration, Beijing, China.

Corresponding author: A.-S. Mériaux, School of Geography, Politics and Sociology, Newcastle University, Claremont Road, Newcastle upon Tyne NE1 7RU, UK. (anne-sophie.meriaux@ncl.ac.uk)

0148-0227/12/2012JB009289

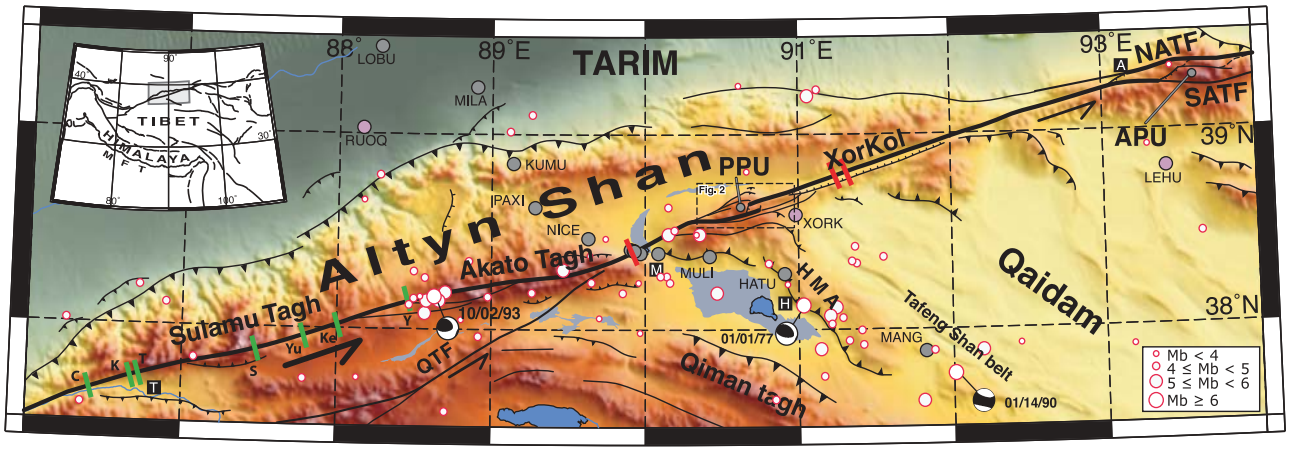

Figure 1. Map of topography and active faulting along Altyn Tagh Fault (ATF) system between 86° and 94°E. Mapping is based on field observations complemented by satellite imagery analysis and earlier work [e.g., *Cowgill et al.*, 2004a, 2004b; *Mériaux*, 2002; *Meyer et al.*, 1998; *Peltzer et al.*, 1989; *Tapponnier and Molnar*, 1977; *Tapponnier et al.*, 2001]. SATF: South Altyn Tagh Fault, NATF: North Altyn Tagh Fault. Grey and purple dots are GPS stations from *Bendick et al.* [2000] and *Wang et al.* [2001], respectively. White dots are earthquakes from USGS/NEIC (PDE), with Harvard focal mechanisms for Mb ≥ 6. Thick green lines indicate published morphological sites at Cherchen He (C [*Mériaux et al.*, 2004; *Cowgill*, 2007]), Kelutelage (K [*Gold et al.*, 2011]), Tuzidun (T [*Gold et al.*, 2009]), Sulamu Tagh (S [*Mériaux et al.*, 2004]), Yukuang (Yu [*Gold et al.*, 2011]), Keke Qiapu (Ke [*Gold et al.*, 2011]) and Yuemake (Y [*Cowgill et al.*, 2009]). Thick red lines indicate trench locations of *Washburn et al.* [2003, 2001] (Kulesayi at ~90°E and XorKol at ~91.25°E). A: Annamba, T: Tura, H: Huatugou and M: Mangnai Zhen. QTF: Qiman Tagh Fault [*Tapponnier and Molnar*, 1977], also named Kadzi Fault in *Cowgill et al.* [2004a]. HMA: Huatugou-Mangnai Anticlinorium. PPU and APU are Pingding Push-Up and Altyn Push-Up (gray lines), respectively. Lakes are in dark blue and salt flats are in pale blue. Studied sites are located along the main branch of the ATF in the Pingding Shan area between 90°E and 91°E. Dashed rectangle outlines area of Figure 2.

studies lead to estimates of 2–17.5 mm/yr, 1.5–17.8 mm/yr [*Gold and Cowgill*, 2011] and 8.5–15 mm/yr [*Cowgill et al.*, 2009], respectively, on the main strand of the Altyn Tagh fault between the Sulamu Tagh and Akato Tagh restraining bends. At ~94.3°E, on the eastern Aksay segment of the north Altyn Tagh Fault (NATF), a slip-rate of 18 ± 4 mm/yr [*Mériaux et al.*, 2004] has been estimated. Three-epoch-campaign GPS results along a profile crossing the fault at Mangnai Zhen (90°E) imply a rate of 9 ± 5 mm/yr [*Bendick et al.*, 2000; *Wallace et al.*, 2004], compatible with broader based, regional campaign GPS studies (9 ± 2 mm/yr [*Shen et al.*, 2001]) (Figure 1). Paleoseismic interpretations of trenches at Kulesayi (~89.9°E) and Xorkol (~91.25°E) suggest a record of only two to three earthquakes with Mw of 7 to 7.6 in the last 2–3 ka, consistent with a slip-rate of about 10 mm/yr [*Washburn et al.*, 2003; *Washburn et al.*, 2001] (Figure 1). A slower slip-rate of ~4 mm/yr had been inferred from an earlier field survey of Quaternary tectonics along the entire length of the fault [*Ge et al.*, 1992]. Recent InSAR studies also yield divergent results. At ~94°E, one study derives a rate of 8–10 mm/yr [*Jolivet et al.*, 2008], while other studies yield slip-rates of 11 ± 5 mm/yr at 85°E [*Elliott et al.*, 2008] and of 5 ± 5 mm/yr on the Karakax Valley segment of the fault near 80°E [*Wright et al.*, 2004]. It is possible that part of the discrepancy between the slow and fast slip-rates stems from the different observational time intervals sampled by each technique [*Chevalier et al.*, 2005; *Mériaux et al.*, 2004; *Van der Woerd et al.*, 2006]. Indeed, GPS and InSAR measurements yield far-field, decadal averages, while morphochronology and trenching address the near-field, centennial and millennial behavior of the fault. In addition, the results of some studies [*Ge et al.*, 1992; *Washburn et al.*, 2001] are constrained by very few absolute ages. Other morphological studies have used only one dated offset riser to derive the slip-rate [*Cowgill et al.*, 2009; *Gold et al.*, 2009], that do not allow the derivation of an averaged long-term slip-rate or to test the variability of the slip rate over time and space. As importantly however, the rather complex geometry of the ATF fault system, related to its propagation toward the NE, along with the growth of the Tibet plateau [*Métivier et al.*, 1998; *Meyer et al.*, 1998; *Tapponnier et al.*, 2001], requires that the three different types of approaches be applied to the same segment of the fault to allow comparison of local slip-rate estimates, which has not been hitherto the case. The simple fact that each study has derived a slip-rate at a given location along the N70°E strike of the ATF and sampled different timescales does not make the comparison of all the slip-rate estimates straightforward.

[3] Here, we document and date cumulative geomorphic offsets and use them to constrain the long term slip-rates at two sites along the foot of Pingding Shan (~90.7°E), north of Huatugou, about halfway between the two trenching areas selected by *Washburn et al.* [2001] and ~60 km east of the

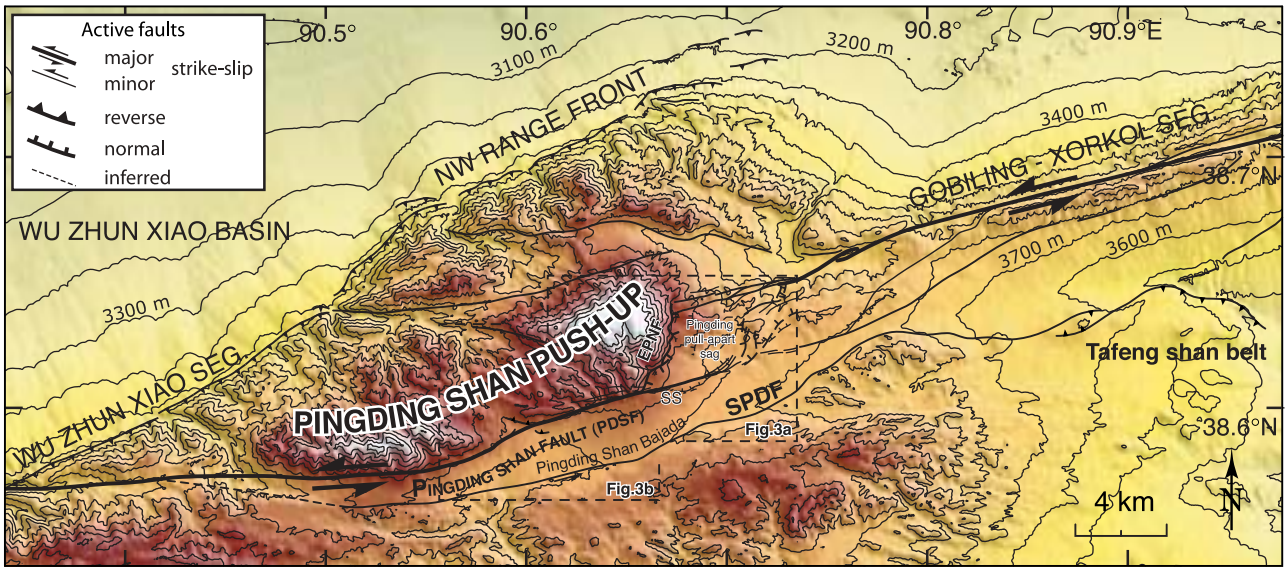

Figure 2. Topography of Pingding Shan push-up, between Wu Zhun Xiao and Xorkol-Gobiling (also named Xorkol-Lapeiquan [*Mériaux et al.*, 2005]) segments of Altyn Tagh Fault system. Elevation are from 1/100 000 scale Chinese topographic maps. DEM Contour elevation are only labeled in nearby bajadas, for clarity, and main contour interval is 100 m. Bold lines are active faults (dashed when less clear); boldest lines, main strands of ATF. Boxes outline areas of Figures 3a and 3b. EPNF: East Pingding Normal Fault; SPDF: South Pingding Fault; SS: south scarp.

Huatugou-Milan GPS profile [*Bendick et al.*, 2000; *Wallace et al.*, 2004] (Figure 1). We targeted this area for morpho-chronologic analysis because of its remarkable series of well-preserved offsets observed on the field and on satellite imagery [*Peltzer et al.*, 1989]. The average values and bounds we obtain should be considered minima for the millennial rate at 90°E, because other splays of the fault run parallel to the main strand studied, and the large Huatugou-Mangnai anticlinorium, which is underlain by active seismic thrusts (Figure 1), meets with the fault southwest of Pingding Shan, which likely decreases the sinistral rate in the manner documented at the Tanghenan Shan junction, between Aksay and Subei [*Mériaux et al.*, 2005; *Meyer et al.*, 1998; *Van der Woerd et al.*, 2001].

2. Quaternary Geology and Geomorphology of the ATF Between 90° and 92°E

2.1. Large-Scale Geometry and Segmentation of the Fault

[4] The 4-km Pingding Shan step is the largest geometric discontinuity along the main strand of the Altyn Tagh Fault between the Akato Tagh and Annanba junctions [*Mériaux et al.*, 2005, Figure 1]. The former junction, at 89.6°E east of the Akato Tagh bend, is located where the Qiman Tagh strike-slip fault [*Tapponnier and Molnar*, 1977], also referred to as the Kadzi Fault [*Cowgill et al.*, 2004b], meets with the central segment of the ATF (Figure 1). The latter junction (92.9E) is where the North Altyn Tagh Fault (NATF) and South Altyn Tagh Fault (SATF) merge, just west of the Altyn push-up [*Mériaux et al.*, 2005, Figure 1]. The Pingding Shan left-step has been identified as a likely boundary for earthquake rupture, even though timing constraints on the dates of the Most Recent Events (MRE) in the Kulesayi and Xorkol trenches [*Washburn et al.*, 2001] are suggestive of event clustering. While the step is presently marked by a 5 km-long composite pull-apart sag, it lies at the eastern end of a much larger feature, the ~40 km-long Pingding range. On a large scale, this mountain range separates the Xorkol-Lapeiquan (also named Gobiling-Xorkol) and Wuzhunxiao segments of the fault (Figure 2) [*Mériaux et al.*, 2005; *Washburn et al.*, 2001]. The range, which corresponds both to an 8–10 km right step between these segments and to a clockwise, ~20°-swing in the average strike of the fault, likely formed as a push-up in a long-lived, first-order restraining bend of the ATF. Thrusting and folding of late Pleistocene bajada fans are particularly clear at the northeastern corner of the push-up (Figure 2). The northwestern range front fault, which extends in direct continuation of the Wuzhunxiao segment of the ATF (Figure 2) also bears evidence of Quaternary oblique thrusting, which has uplifted alluvial fans. The SW extremity of the Xorkol segment of the fault, on the other hand, splays and steps southwards toward the Pingding Shan southern range-front fault, which is more closely aligned with the N70°E average strike of the ATF (Figure 2).

[5] There is evidence for complex, Pleistocene and active faulting within the Pingding Shan push-up. The traces of the most conspicuous faults strike roughly east–west, parallel to bedding trends in the strongly folded Paleozoic sediments (Figure 3) [*Jiao et al.*, 1988], indicative of oblique thrusting and bedding-slip, as well as probable horizontal bookshelf faulting (Figure 2). Such internal oblique faulting, and the extensional step with active normal faulting at the eastern end

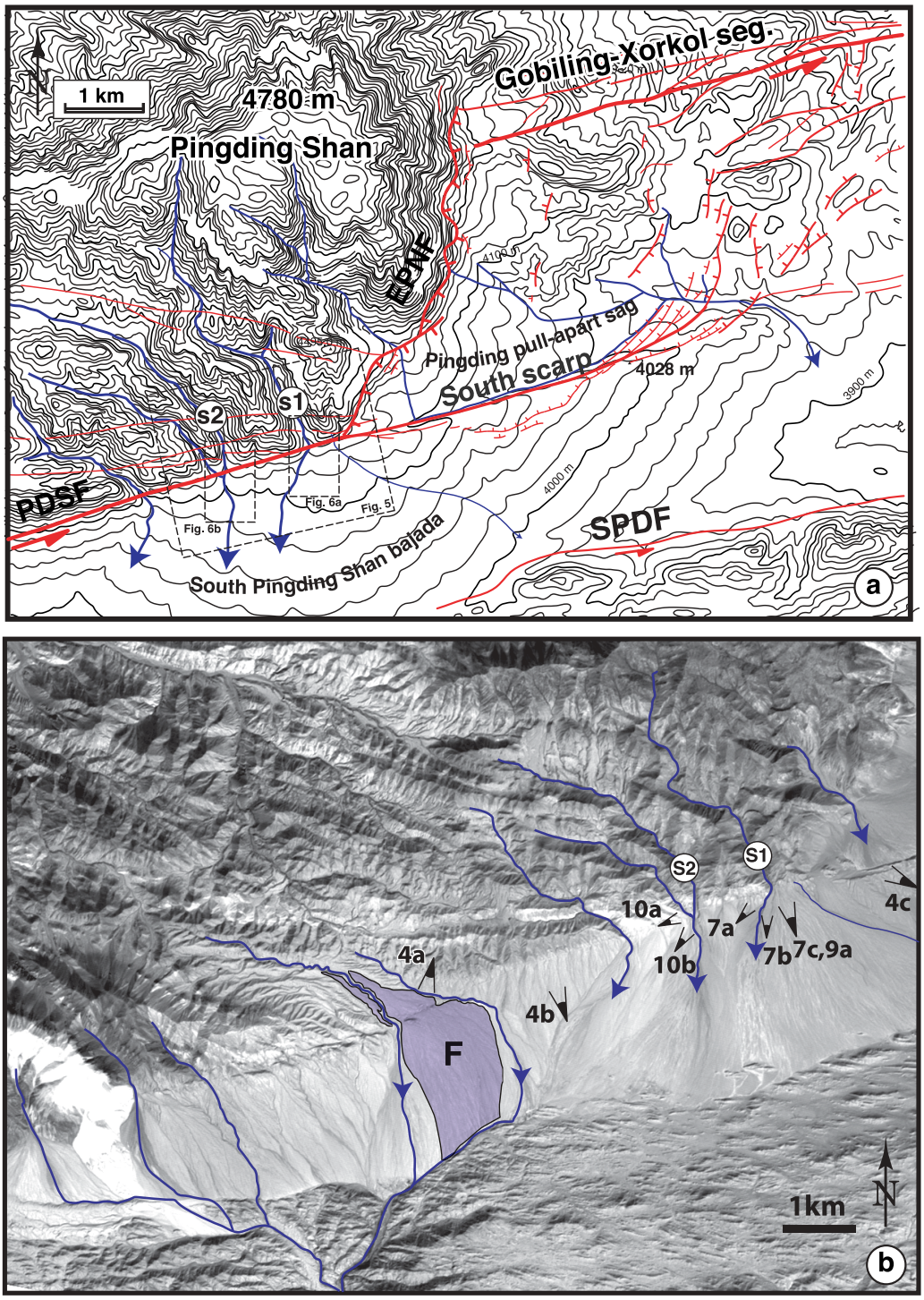

Figure 3. (a) Active faulting around East Pingding Shan pull-apart, projected on 1/100 000 scale topographic map contours, contour interval is 20 m. S1 and S2 are streams at studied sites. PDSF: Pingding Shan Fault, EPNF: East Pingding Normal Fault and SPDF: South Pingding Fault. (b) Point of view of photographs in Figures 4a–4c, 7a–7c, 9a, 9b, and 10a are indicated on Spot Image (KJ 228–272, 27/10/1986). Light purple is wide fan (F) west of S1 and S2 (see discussion in text). Note that frame b is offset to the west with respect to frame a (see Figure 2 for location).

of Pingding Shan, are comparable to the deformation we mapped farther east across the Altyn push-up [*Mériaux et al.*, 2005]. Both of these transpressional bends appear therefore to be in the process of being short-cut by the active fault system.

[6] In the area around 90.5°E, another active sinistral fault parallels the Pingding Shan Fault strand (PDSF) to the south, for at least 40 km (Figures 1, 2, and 3). The South Pingding Fault (SPDF), follows the distal edge of the southern

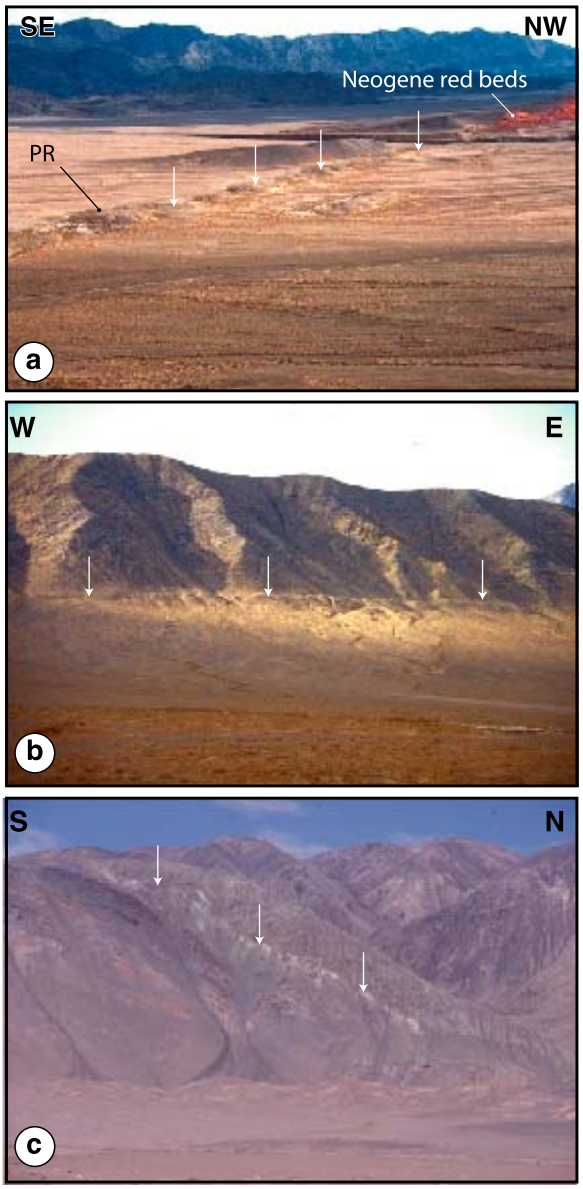

Figure 4. (a) North-looking view of cumulative pressure ridges along PDSF across ~800 m-wide fan (F) (see Figure 3). Note deformed Neogene red beds capped by south-dipping Quaternary conglomerates in background. PR points to one particularly large cumulative pressure ridge. White arrows point to active PDSF trace. (b) Shutter ridges, and stream channels offset by ATF main strand along Pingding range-front west of S2. Arrows indicate active trace of PDSF. (c) Northwestward-looking picture of the EPNF. Note the whitish fault trace showing a fresh rupture on a secondary fault (N80°E) affecting the bedrock of the Pingding Shan.

Pingding Shan bajada (Figure 2), bounding the strongly folded and left-laterally sheared Jurassic shales south of it [*Jiao et al.*, 1988]. SPDF is marked by meter-high scarps that cut most of the terraces deposited and incised by the streams that flow across its trace. Like several other similar faults bifurcating southeastward away from the main ATF trace east of 91°E, this splay-fault appears to transfer slip to thrusts, here principally to those which underlie the Tafeng Shan belt, a series of large, growing anticlines in the Qaidam basin, east of the Huatugou-Mangnai anticlinorium (HMA, Figure 1) [*Mériaux et al.*, 2005; *Meyer et al.*, 1998].

2.2. Local Geometry of Active Faulting Around the Southeast Corner of the Pingding Shan

[7] For over 10 km west of the Pingding left-step, the main strand of the ATF (i.e., PDSF) marks the base (at ~4140 m a.s.l.) of the rectilinear, southern front of the Pingding range, with a ~N70°E strike, similar to that of the Xorkol segment (Figures 2 and 3). About halfway along this stretch of the Pingding segment of the fault, a large valley floored by a broad fluvial fan (F, Figure 3) divides the highest part of the range into two distinct massifs with characteristic whaleback-shape and EW elongation, roughly parallel to the steeply dipping bedrock strata. The morphology and trend of these mountain massifs, especially of the western one, suggests that they formed as *en-échelon* basement ramp-anticlines [e.g., *Meyer et al.*, 1998], due to Cenozoic, oblique-sinistral motion along the fault.

[8] Immediately west of alluvial fan F, the ATF juxtaposes the Ordovician metasedimentary basement with deformed Neogene red beds unconformably capped by south-dipping Quaternary conglomerates (Figure 4a) [*Jiao et al.*, 1988]. Across the ~800 m wide surface of the fan (Figure 3b), 5–10 m-high, left-stepping pressure ridges mark the principal active trace of the fault, reflecting repetitive, localized folding of the fanglomerates due to several large earthquakes (Figure 4a). East of the fan, along the mountain base, the PDSF cuts and offsets small range-front catchments, producing local shutter ridges (Figure 4b). The fault also cuts the outlets of three larger stream valleys (Figure 3), thus displacing inset terrace risers downstream from the fault relative to the deeply incised canyons upstream. The two easternmost canyon outlets (S1, S2), closest to the Pingding pull-apart step were targeted for detailed mapping, total-station measurements, and CRN dating (Figures 3, 5, and 6).

[9] As PDSF reaches the Pingding pull-apart, the fault divides into two strands marked by large Quaternary cumulative scarps. One strand, the East Pingding Normal Fault (EPNF), veers abruptly ~45° northwestward from the average strike of the PDSF, following the base of 300–600 m-high triangular facets whose apexes reach the flattish, abraded surface that locally tops the Pingding Shan at 4780 m a.s.l. (Figures 2 and 3). The second, dominantly strike-slip strand (South Scarp, SS, Figures 2 and 3) steps by less than 40 m southwards and continues rectilinearly 5 km eastward (~70°E), all the way to the opposite end of the pull-apart sag. These two faults mark the well-defined, western and southern edges of this asymmetric pull-apart (Figure 3a).

[10] We found fresh pressure ridges and free-faced scarps not only along the PDSF west of the pull-apart sag and along the southern stretch of the EPNF but also along SS, previously identified as an inactive Quaternary fault [*Washburn et al.*, 2001]. Other fresh free-faced seismic scarps cut basement rocks within the range (Figure 4c). Thus, not only are the three main faults of the area active, but all of them, and other secondary basement faults as well, ruptured during recent seismic events. Late Pleistocene and active slip on the

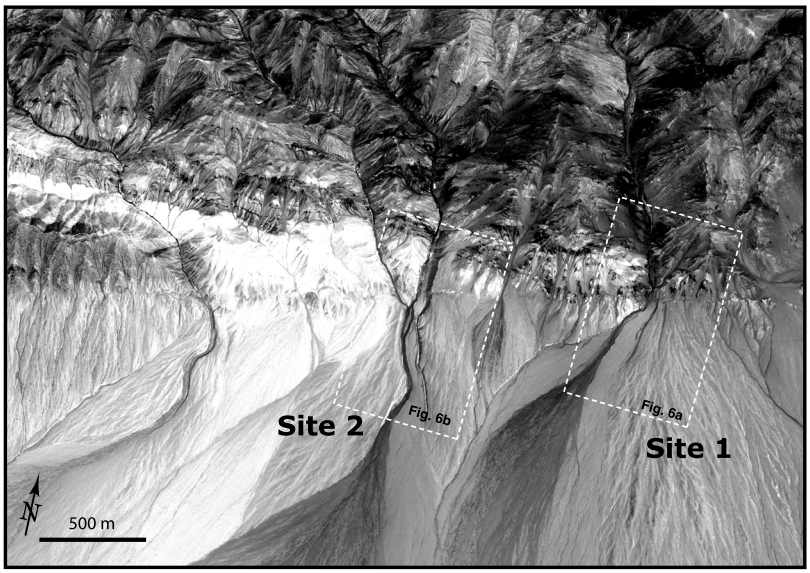

Figure 5. High-resolution Quickbird satellite image (pixel size 60 cm) of site 1 and 2, along streams S1 and S2, respectively. Boxes outline Figures 6a (site 1) and 6b (site 2).

EPNF and SS are quantitatively documented in *Mériaux* [2002].

3. Terrace Surfaces and Sinistral Terrace Riser Offsets at Sites 1 and 2

[11] The Quaternary geomorphic settings of the outlets of streams S1 (Site1) and S2 (Site 2) onto the south Pingding bajada across the PDSF are broadly comparable (Figures 5, 6, and Figures S1 and S2 of the auxiliary material), although one tributary stream merges with the western stream (S2) about 50 m south of the fault trace.[1] Two large composite fans, whose apexes lie a few tens (S1) and a few hundreds of meters (S2) north of the fault, spread out southwards from the two stream valleys. The fans are composed of inset terraces separated, near the range-front, by well-defined risers whose heights decrease toward the south (Figures 5 and 6).

[12] As shown on the photographs of Figures 7 and 8, the terrace surfaces are remarkably planar and mostly devoid of loess cover. They are uniformly paved with angular pebbles and small cobbles (4–10 cm) in a silty matrix (Figure 7). There are no rodent holes, no evidence for cryoturbation, and no visible salt crusts. Nor is there any direct evidence for surface clast fragmentation. Primary channels are visible on the main terrace surfaces (e.g., T1, site 1, and T3, site 2, Figure 7 and 8b) but their geomorphic expression is subtle, and depth generally less than 20 cm. As clear on the field photographs, the aspect of the 3 abandoned fluvial terraces (T1, T2, T3) at site 1 is similar despite their different heights, hence relative abandonment ages. The main difference is that T1 has a denser network of better preserved primary channels and resembles most the present-day active riverbed, whose surface is somewhat rougher, with looser cobbles. This implies that some degree of cobble fragmentation and cementation, both involved in terrace surface smoothing with age, occurred. We found little evidence for terrace erosion, hence surface younging, in particular by regressive channels, on any of the terrace surfaces at either site, except very near the largest risers or fault scarps. At site 1, a thin layer of washed silt has ponded at places on T1, particularly in a channel along the base of the T2/T1 riser. Small tufts of grass have locally exploited the soil and moisture traps thus formed (Figure 7b). At site 2, the proportion of washed silt is larger, as visible on the field photographs (Figures 8b and 10), but surface pebbles are nevertheless abundant. Also, there appears to have been some local deposition of colluvium derived from the range front atop of the highest terraces (T3′, T4) close to this front (Figures 6b and 10b). Nevertheless, provided that the few areas where the surfaces might have been altered by the above processes be avoided, which we carefully did, the terraces at either site appeared to be almost ideally suited for CRN dating.

[13] The terrace risers on the left (east) bank of the streams reach the fault trace, which is locally marked by a south-facing, 2–4 m high scarp, *en échelon* pressure ridges, but also by upslope-facing scarps at places. Such risers thus provide rather clear piercing points (Figures 5, 6, 9 and 10). In the fairly steep-sided valley upstream from the fault, only narrow residual benches of the uppermost terrace levels (T2, T3, T3′, T4), in part mantled with colluvium, are preserved. In both valleys, the best preserved upstream benches are on the left banks of the streams, and have been deeply incised by tributary gullies, as well as eroded by lateral cutting of the streams (Figures 5, 6, 9, 10, and 15). The upstream T3′ bench is up to 70 m-wide in the valley of S2, but too narrow for sampling in that of S1 (Figure 6b). All the upstream residual terrace benches are thin straths, with risers showing free faces in both terrace gravels and bedrock underneath.

[1] Auxiliary materials are available in the HTML. doi:10.1029/2012JB009289.

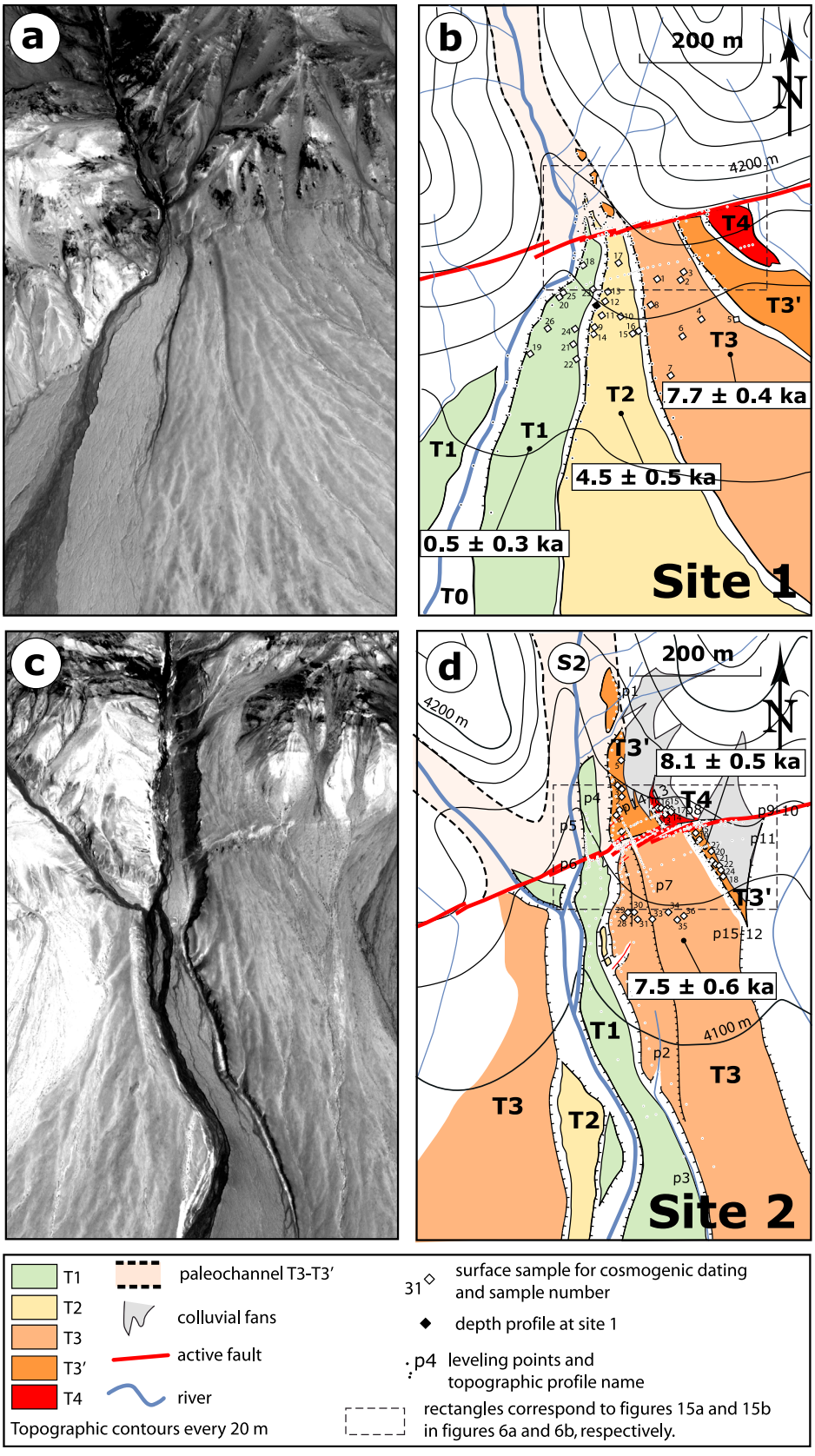

Figure 6. (a and c) are enlargement of Quickbird image of areas corresponding to Site 1 and 2, respectively. (b and d) are geomorphic interpretations of Site 1 and 2, respectively. Total station profiles, terrace levels, samples numbers are indicated. Terrace colors, from green to red, indicate increasing height, hence relative age. Mean CRN model ages are also indicated.

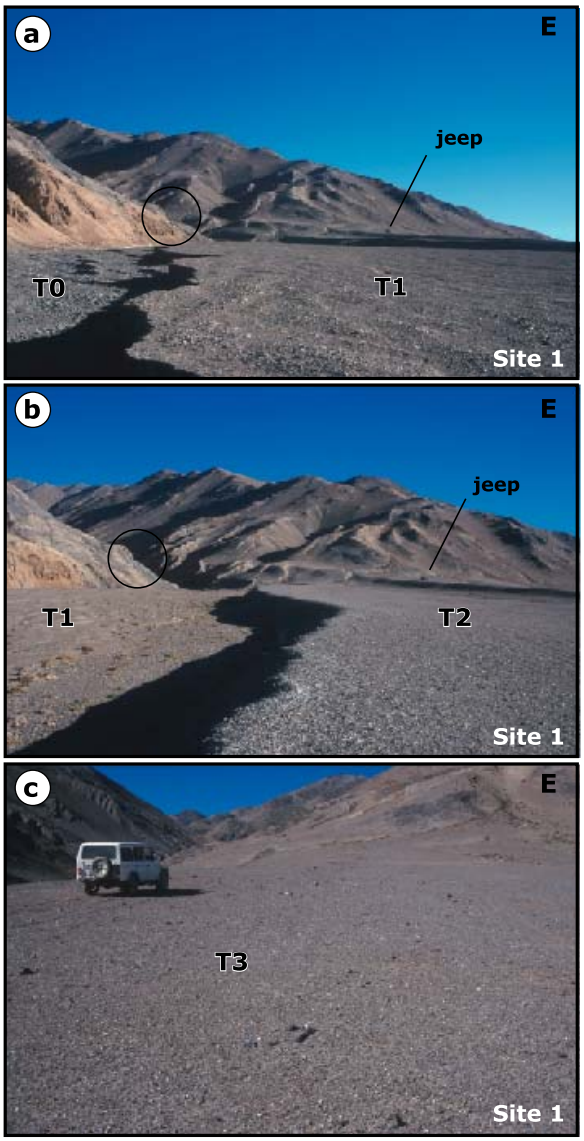

Figure 7. Pictures showing the surface morphology of three main terrace levels (a) T1, (b) T2, (c) T3 at site 1.

[14] To quantify the cumulative-offsets of the risers and the morphology of the different terrace levels (relative heights, slopes, …), total-stations profiles were leveled at both sites using a theodolite (Wild T2000, DI3000). The technique followed is that pioneered by *Peltzer et al.* [1988], and used repeatedly since by our group [e.g., *Gaudemer et al.*, 1995] and by others. Instrumental errors (a few cm at most) are negligible for the problems of interest here. Given the sharpness of even the oldest riser crests at either site, the horizontal positions of all data points are defined with a precision of less than 1 m. Total-station elevation profiles of the risers and streambeds, projected on vertical planes perpendicular to the local fault strike (N163°E for S1 and N160°E for S2, Figures 11 and 12), show that, near the fault, the streams have incised up to 15 to 20 m into the highest terraces in both valleys (Figures 11–15). The amount of incision decreases fairly rapidly and uniformly downstream, as the upper terrace treads slope more than the lower ones (4–5° versus 2.5–3°) but there is no prominent, discrete step at the fault on the later. At site 1, T1, the lowest abandoned terrace, 1 to 2 m above the active flood channel sublevels, shows no vertical offset. At site 2, the trace of a metric pull-apart, apparently smoothed out by flooding, is visible on T1. This implies that the average long-term vertical component of throw on the fault is small enough to be neglected, and that the vertical offsets visible along the fault trace on the higher terrace treads are apparent offsets resulting from strike-slip displacement and local, shallow seismic warping and folding (mole tracks). This inference is supported by the observation that the surface of the broad fan (F, Figures 3b and 4a) disrupted by the large cumulative mole-tracks to the west (Figure 4a) shows no significant vertical offset either.

[15] In both valleys, the T1/T0 risers, in spite of their 1–2 m heights above the active river channels are not offset sinistrally by the fault (Figures 9 and 10). This might be either because there has been no earthquake since the risers formed or because fast lateral cutting by the streams flowing on T0 prevents preservation of incremental, lateral seismic offsets of these lowermost risers. The fossil risers (T2/T1, T3/T2, T3′/T3, T4/T3′, T3/T1, T3′/T1), by contrast, record cumulative lateral offsets whose amounts increase, as expected, with elevation above T1 (Figure 15, Table 1, and Figures S1 and S2 of the auxiliary material).

[16] In the valley of S2, a near vertical, 13 to 20 m-high cliff bounds the west-side of the highest terrace levels (T3′, upstream, and T3, downstream from the fault) (Figures 10, 12, and 14). Since the terrace level at the base of this cliff is T1, part of the cumulative displacement record (T2) is missing. This is not the case downstream from the outlet of S1, where the T2/T1, T3/T2 and T4/T3 risers are well defined, the clearest and highest ones being T2/T1 and T3/T2 (4 and 5 m- high, respectively, Figures 6a, 11, and 13).

[17] At either site, the offsets of the terrace riser's tops and bases have lower and upper bounds defined by the corresponding upstream and downstream terrace piercing lines intersecting the fault's right-stepping surface scarp (each piercing point is marked by a capital letter on Figures 15a, 15b, and Table 1). The largest offsets are along the main fault scarp, but smaller additional displacements are visible along off-shooting secondary surface breaks (Figure 15). The minimum and maximum offset of each terrace tread is defined by the intersection of the fault trace with the eastern and western terrace edges, also defined as the base of the upper riser and the top of the lower riser, respectively, upstream and downstream of the fault (Table 2). For instance, the offset of the terrace level T2 is bracket by the minimum offset riser **T2**/T1 at its top and by the maximum offset riser T3/**T2** at its base. All piercing points are defined using total-station measurements and the high-resolution Quickbird image (60 cm pixel) and are projected onto the local, average direction of the main fault trace (N73°E at site 1, N70°E at site 2) (Figure 15). All piercing points are defined with a resolution of 4 m as illustrated by the size of the symbols on Figure 15, so all the offsets defined below are defined at ±8 m. The stepwise reconstructions of progressive left-lateral displacements and stream incisions are shown at site 1 and site 2 in Figures S1 and S2 of the auxiliary material, respectively.

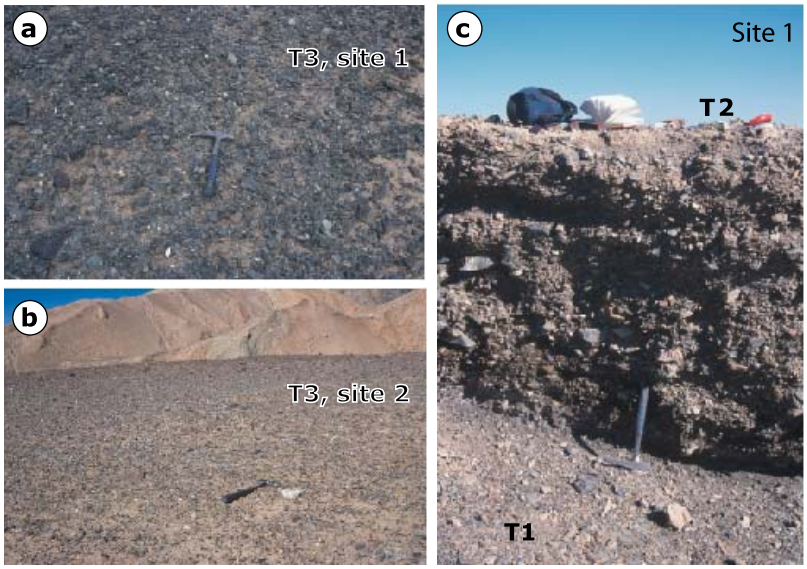

Figure 8. Close-up photographs of typical terrace T3 surface aspect at sites (a) 1 and (b) 2. (c) Stratigraphy showing usual pebbles and clast sizes, amount of silt and variation with depth at location of depth-profile at site 1 in terrace T2.

[18] At site 1 (Figure 15a and Figure S1 of the auxiliary material), the offsets of the western and eastern risers of terrace T1 are 0 m (BI) and 13 m (CJ), respectively. Although such offsets are evidently not coeval, they represent the actual lower and upper bounds of the offset of the terrace tread itself (Table 2). The corresponding offsets and bounds for T2 are 15 m (DK′) and 38 m (EL′). For T3, the northern piercing point of the western, upstream riser must have been located at the approximate height of T3 between E and F. The southern piercing point is that between the top of the T3/T2 riser and the main fault scarp (M′). The lower bound of the T3 offset tread is thus 26–44 m (EF-M′). To first order, the upper bound should be comparable to the offset of the top of T3′/T3, i.e., 101 m (OF), although it might be even greater, at most 122 m (GP), since there is no remnant of T3 north of the fault. Note that this maximum offset reconstruction of T3 brings the western riser of T3 (M) 122 m to the west of its present position, a position still compatible with the width of the valley at the level of T3 (Figure 6 and Figure S1 of the auxiliary material). For T4, the offset range from 122 m (HQ) to an undefined maximum, at least as the easternmost extension of the terrace (R) and thus, greater than 179 m (HR).

[19] As at site 1, the bounds of the offsets of the terrace treads T1, T3 and T3′ on the left bank of S2 are defined by matching their eastern and western risers north and south of the fault (Figure 15b and Figure S2 of the auxiliary material). For T1, which is preserved upstream and downstream of the fault, such bounds are 0 m (CM) and 20 m (D′N′), respectively (Table 2). The lower bound of the offset of the terrace tread T3′, which has a well-defined western riser on either side of the fault is 118 m (F″R). The upper bound, on the other hand, can only be loosely estimated to be 148 m (TI), (Figure 15b). Since terrace tread T3 has no counterpart north of the fault, bounds on its offset can only be roughly estimated, as at site 1. Following the same line of reasoning, one obtains a lower bound of 22–44 m (D′F′-P) and an upper bound of 118 m (F′R), or even as much as 148 m (TI) would be plausible, and possible, respectively.

4. Cosmogenic Radionuclide Dating of the Fluvial Terraces

4.1. Site 1

[20] We collected 26 quartz-rich embedded cobbles on the surfaces of T1, T2 and T3 (8 to 10 on each surface) on the east bank of S1, downstream from the fault, for CRN dating (Figures 6b and 16, and Table 3). Five cobbles were also collected from a free-face of the T2/T1 riser, which we rejuvenated, but only two of these samples contained enough quartz to be analyzed (Figure 8c).

[21] Table 3 presents the ^{10}Be and ^{26}Al CRN model ages obtained on the main terrace levels (T1, T2 and T3). The ^{10}Be ages younger than 20 ka (26 out of 28 values) are plotted on Figure 16, together with normal kernel density estimate (Psum) for all dated samples, which may be written as:

$$P_{sum}(t) = \sum_i e^{-\left(t-a_i^2\right)/2\sigma_i^2} / \sigma_i \sqrt{2\pi} \qquad (1)$$

where t is time, a_i is the exposure age of sample i and 2 σ_i is the reported error [*Daëron et al.*, 2004; *Lowell*, 1995; *Taylor*, 1997]. We followed standard chemical processing of the samples [*Kohl and Nishiizumi*, 1992] and surface exposure ages were calculated similarly to the CRONUS-Earth calculator v2.2 modified from *Balco et al.* [2008] using the *Lal* [1991] and *Stone* [2000] scaling factor, a constant production rate of 4.49 ± 0.39 atoms/g of SiO_2, the Be half-life of 1.387 ± 0.012 Ma [*Chmeleff et al.*, 2010; *Korschinek et al.*, 2010], a density of 2.6 g/cm^3 and an attenuation length of 177 ± 4 g.cm^2 [*Farber et al.*, 2008] (Tables 3 and 5, and Tables S1 and S2 of the auxiliary material). All the quartz

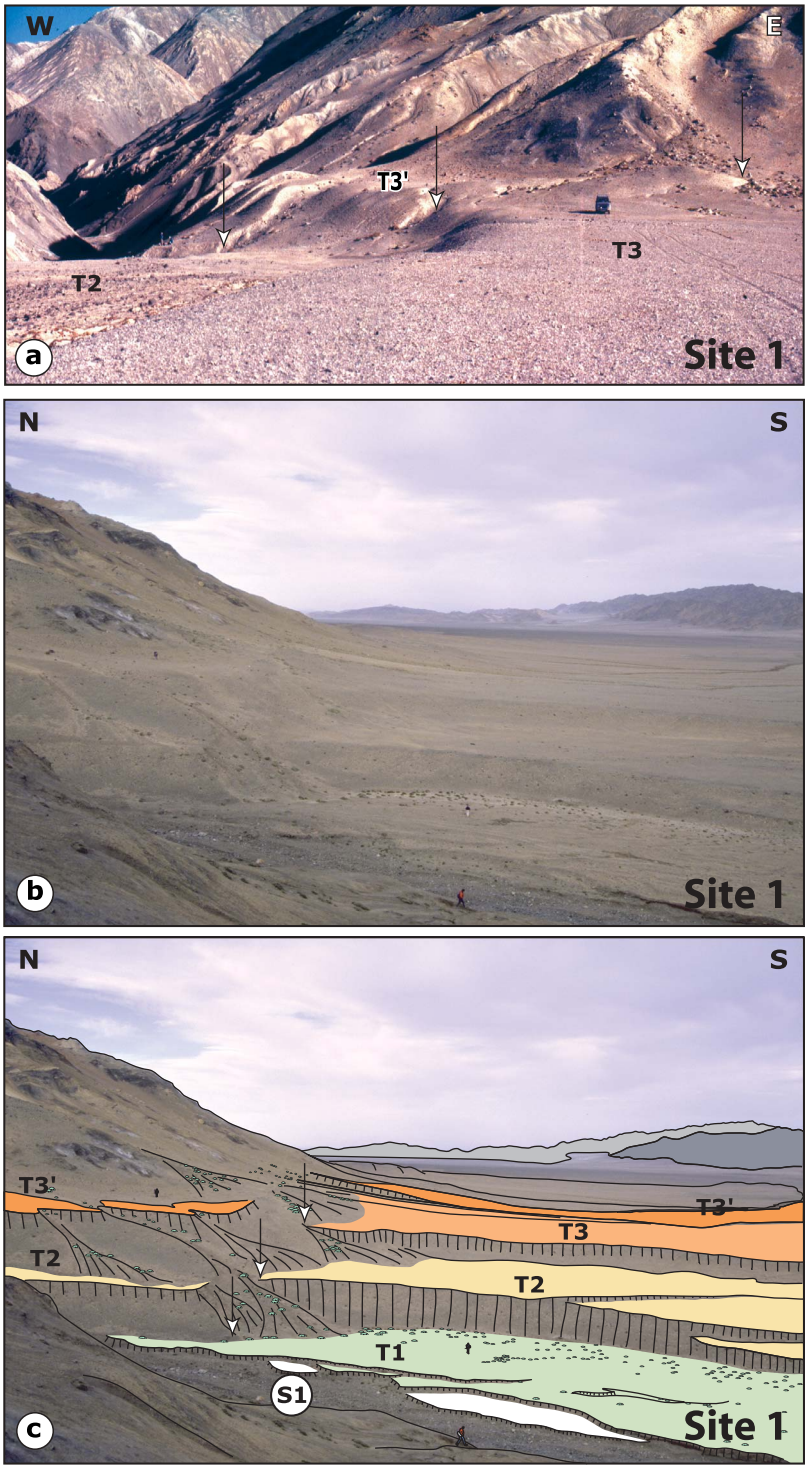

Figure 9. (a) North-looking view of offset terrace risers at site 1. (b) East-looking, fault-parallel view of main Pingding strand of ATF offsetting terrace risers at site 1. (c) Interpretation of the picture in 9b with same coloring for the different terrace levels as for 6a.

cobbles dated (8 on T3, 9 on T1 and 11 on T2, among which the two subsurface samples) yield concordant model ages, with an $^{26}Al/^{10}Be$ age ratio of ~0.95 on average. Despite such concordance, the discussion below is based on the ^{10}Be CRN model ages, which are in general slightly older than the ^{26}Al CRN model ages [*Mériaux et al.*, 2004, 2005].

[22] On all three terraces, the ^{10}Be CRN model ages group into clusters with distinct outliers (Figure 16, and Tables 3 and 4). Both clusters and outliers are defined using simple rules. In particular, all values with overlapping errors bars are considered to be part of a cluster. The outliers identify by this simple rule are then tested via the Chauvenet's statistical

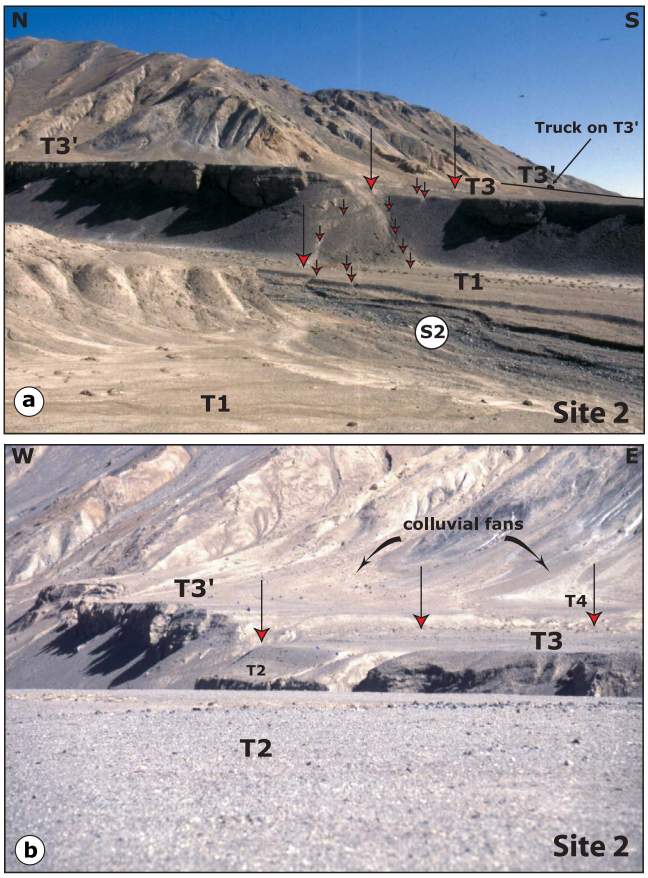

Figure 10. (a) East-looking view of offset terrace risers at site 2. (b) North-looking view of Main Pingding strand of ATF offsetting terrace risers at site 2. Note well-lit fault scarp between T3 and T3′.

criterion, which is a widely accepted method that assesses the probability of finding a datum differing markedly from the average [see *Bevington and Robinson*, 2002 p. 58]. Application of the Chauvenet's criterion may imply several iterations depending on the number of outliers. The results of Chauvenet's criterion to the terrace's age populations are shown in Table 4.

[23] On T3, the eight ^{10}Be CRN model ages range from 7.14 ± 0.69 ka to 32.42 ± 2.97 ka, yielding a mean and standard deviation for the whole population of 14.3 ± 11.1 ka with a mean squared weighed distribution (MSWD) of 20.6. The first iteration of Chauvenet's criterion readily isolates as outliers the two samples with ages of about 30 ka, reducing the mean of the remaining population to 8.3 ± 1.7 ka with a much smaller MSWD of 2.3. The second iteration separates QGQ-8 (11.65 ± 1.08 ka) as another outlier. The resulting mean age of the five remaining samples after this final iteration is 7.7 ± 0.4 ka with a MSWD of 0.3, which is typical of a normally distributed population. Note that these sample CRN model ages form a rather tight cluster, with an age spread of only 1 ± 0.5 ka.

[24] On T2, the ^{10}Be CRN model ages of the 9 surface samples range from 4.03 ± 0.37 ka to 10.66 ± 0.99 ka. The mean and standard deviation for the entire population is 5.9 ± 2.7 ka with a MWSD of 10.3. The two older samples at ∼10 ka are separated as outliers by one iteration of Chauvenet's criterion, reducing the mean of the remaining population (7 samples) to 4.5 ± 0.5 ka, with a MSWD of 2.5, only slightly larger than that of a Gaussian distribution (Figure 16, and Tables 2 and 3). The only two dated samples in the T2/T1 depth profile have model ages of 4.5 ± 1.3 and 3.2 ± 0.7 ka. The latter is younger than the youngest surface sample. Since the age of the surface cannot be older than the youngest sample at depth [*Ryerson et al.*, 2006], a mean inheritance of about 1.3 ka might be inferred (mean of the surface sample ages minus age of the youngest depth sample). A minimum inheritance of ∼820 years may similarly be derived from the difference between the ages of the youngest sample at depth and at the surface, assuming no inheritance on the depth sample. To go a step further, we use the Monte Carlo simulator of *Hidy et al.* [2010] to derive a model age for T2 from the depth profile samples correcting for both inheritance and erosion (Figure S3 of the auxiliary material). The simulator yields a most likely minimum and maximum values of 1.5 ka and 3.5 ka, respectively, with a lowest Chi-square for 2.4 ka (Figure Sup 5). Clearly however, two depth samples are insufficient to reliably estimate inheritance, especially in view of the variability of the inheritance inherent to the single cobble sampling strategy [*Ryerson et al.*, 2006] and the errors built in CRN model ages at depth, which imply knowledge of the density of the stratum above the sample and of the attenuation of the cosmic ray flux whose estimates vary from ∼140 to ∼180 g/cm^2 [*Gosse and Phillips*, 2001]. Here, we used 177 ± 4 g/cm^2 [*Farber et al.*, 2008] for the attenuation length and 2.2 ± 0.2 g/cm^3 for the overburden density to calculate the two depth-sample model ages and to run the Monte Carlo simulations [*Hidy et al.*, 2010]. It is unfortunate that other depth profile samples had to be set aside after the early stage of chemical preparation due to low yields of clean quartz before dissolution, illustrating the challenge associated with obtaining depth profile data on very young surfaces without amalgamated samples (<5 ka). Despite such reservations, there appears to be some amount of inheritance on T2. As for T3, the T2 sample cluster shows a fairly tight age distribution (<2 ka) as shown by the MSWD of 1.2 of the defined cluster (Table 3). Yet, a mean inheritance of 1ka or 2ka would affect the age of the terrace by 22% or 44%, respectively, given the "young" age of the cluster at 4.5 ka.

[25] On the lower terrace level sampled, T1, the CRN model age distribution of the 9 samples ranges between 0.18 ± 0.05 ka and 3.51 ± 0.33 ka. The mean and standard deviation of the entire sample population is 1.2 ± 1.2 ka with a MSWD of 38.7 reflecting the fairly large age dispersion. Six of the samples are very young (189–810 ka). They may be considered to define the abandonment age of this terrace (mean age: 0.5 ± 0.3 ka; Figure 16 and Table 2) or, at the very least, the time when it was last invaded by centennial floods, as observed elsewhere [e.g., *Mériaux et al.*, 2005; *Van der Woerd et al.*, 1998]. Chauvenet's criterion does lead to the exclusion of the 3 oldest samples but the MSWD remains as high as 16.0. Clearly, the age of T1 is the least constrained of all by the CRN dating measurements at site 1.

4.2. Site 2

[26] Thirty quartz-rich embedded cobbles were dated on the relatively high-level surfaces of T3, T3′ and T4 on both

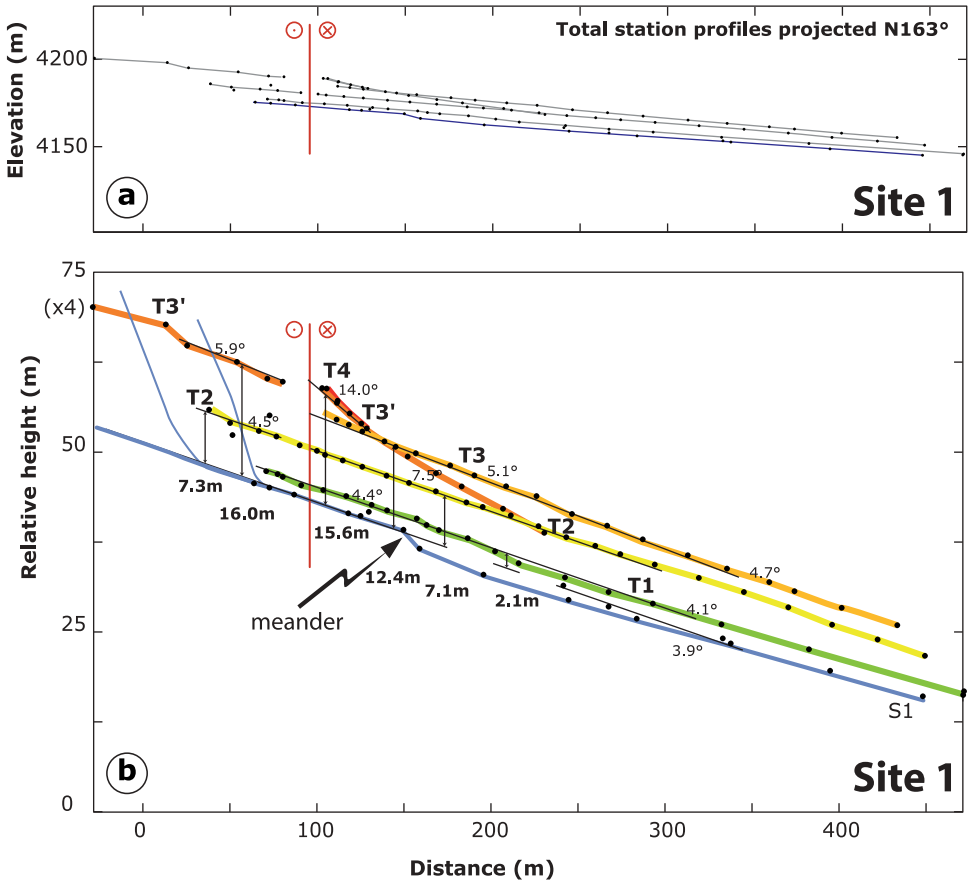

Figure 11. Site 1. Projection of total station profiles at high angle to fault on N163°-striking plane perpendicular to local fault strike. (a) A 1 × 1 scale projection. (b) Projection with vertical exaggeration of four is used to display heights of terraces above streambed and slope of terraces. More than 15 m of incision occurred near the fault. Note that the terraces are not vertically offset by the fault.

sides of the fault on the left-bank of S2 (Figures 6d and 16, and Tables 4 and 5). Table 5 shows all the ^{10}Be CRN model ages obtained (^{26}Al concentrations were not measured for these samples). The CRN data analysis using Chauvenet's criterion is presented in Table 4. The ages younger than 20 ka are plotted on Figure 16. It is immediately apparent that the dispersion of ages is greater than on the S1 terraces. This may result from the fact that the terrace levels sampled on the left bank of S2 are only separated from one another by risers and a scarp of more modest heights (1 to 2.5 m only) than on the left-bank of S1. Also, these high surfaces are rather smoothly connected to the colluvial slopes at the base of the ridges north of the fault, and analysis of the Quickbird satellite images suggest partial invasion by colluvial deposits derived from the later (Figures 5, 6, and 10).

[27] On T4, the CRN model ages of the 7 dated samples upstream from the fault show the greatest dispersion of our study with values ranging from 4.39 ± 0.57 ka to 27.15 ± 0.49 ka, leading to a mean and standard deviation of 13.5 ± 7.7 ka, with a MSWD of 26.6. Two iterations of the criterion define 3 outliers (27.2 ka, 18.5 ka and 4.4 ka) reducing the mean and the standard deviation to 11.1 ± 3.5 ka with a MSWD of 10.4, far from that a normally distributed population. Indeed, this cluster has two samples close to 8 ka, comparable to the age of the T3 levels at either site, and two other samples with ages between 12.5 and 15.5 ka (Table 5). These latter values might be taken as representative of the abandonment age of this highest terrace, which has to be older than T3′, but the absence of clustering in the data make this inference very weak. In fact, the age data we obtained so far is insufficient to date T4.

[28] The two other terrace levels (T3, T3′), whether up- or down-stream, yield a majority of CRN model ages between 5 and 11 ka (17 out of 23) with 6 clear outliers, readily eliminated by Chauvenet's criterion, showing much older model ages (3 ages around 16–17 ka, and 3 ages >25 ka, Table 5). These two levels, which stand above S2 at the same elevation as does T3 above S1 at site 1 (11 ± 0.5 m to 15.7 ± 0.2 m) are thus essentially coeval with the latter.

[29] At a more detailed level, on the slightly lower terrace (T3) downstream from the fault, the 8 samples collected have CRN model ages with a mean and standard deviation of 10.7 ± 4.3 ka, and a MSWD of 10.8. Two iterations of Chauvenet's criterion separate 4 outliers (Table 3), reducing the mean and standard deviation of the 4 remaining clustered sample ages to 7.5 ± 0.6 ka, with a MSWD of 0.8, typical of a normally distributed population. Note that the resulting ages of the two T3 cluster at sites 2 and 1 then become identical within error, consistent with the terrace's similar heights above the streams.

[30] On T3′, the 15 samples collected both upstream and downstream from the fault show much greater spread, with

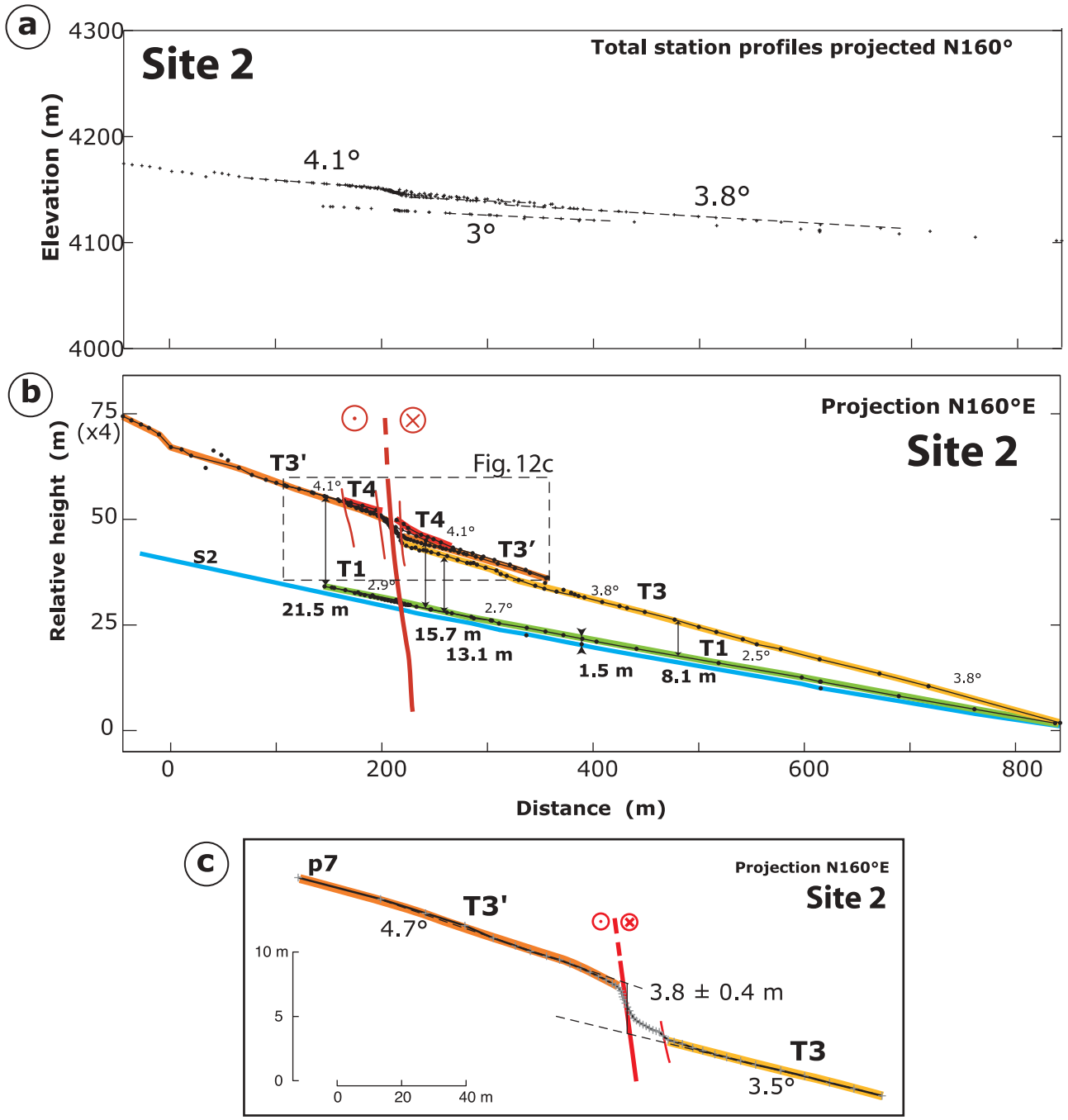

Figure 12. Site 2. Projection of total station profiles at high-angle to the fault on N160°-striking plane perpendicular to local fault strike. (a) Average south slope is indicated on 1 × 1 scale projection. (b) Projection with vertical exaggeration of four shows heights of terraces above streambed. Incision amounts are comparable to those at site 1 south of the fault, but are larger north of the fault due to local vertical displacements. (c) Height of steep main fault scarp separating T3′ and T3 along profile p7 (see discussion in text).

CRN model ages ranging from 5.12 ± 0.14 ka to 33.24 ± 1.08 ka, a mean and standard deviation of 12.6 ± 9.5 ka and a MSWD of 19.6 (Tables 3 and 4, and Figure 16). Three iterations of the criterion remove 5 outliers (30.2 ka, 30.9 ka, 26.6 ka, 16.3 ka and 10.0 ka) from the population. We note that aside from these older outliers, the CRN model ages of the T3′ samples upstream have 4 distinctive younger samples than on T3. These results combined with the presence of colluvium deposits on this terrace illustrate the possible post-contamination of the upstream surface that may bias the dating of T3′ toward younger ages. Leaving aside these data, the mean and standard deviation of the 6 remaining CRN model ages converge to 8.1 ± 0.5 ka, with a MSWD of 0.4, typical of a normally distributed population (Table 3). Within error, this age is thus undistinguishable from that of T3, which indicate that the two terraces, which are

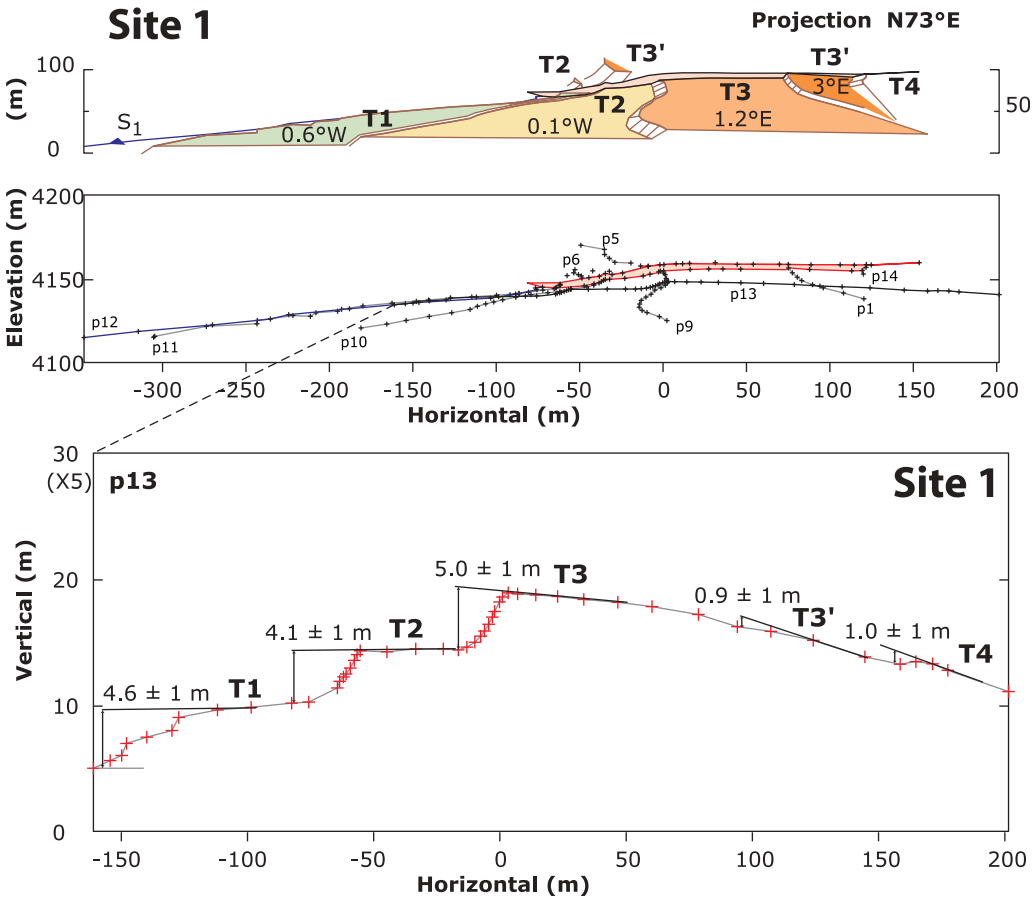

Figure 13. Site 1. Projection on locally N73°-striking fault plane of total station profiles. (top and middle) Average slopes of each terrace surface are indicated on 1 × 1 scale projection. (bottom) Projection with vertical exaggeration of five of downstream profile p13 parallel to fault strike outlining the fan shape terraces. Relative heights of terrace risers are indicated.

morphologically separated only by a 1.6 m high riser downstream from the fault and the 3–4.6 m-high fault scarp (Figures 9 and 11) were indeed abandoned roughly at the same time, even though T3′ is slightly older than T3.

5. Interpretation: Bounds on the Ages, Offsets and Slip-Rates

[31] Overall, 52 of the 58 samples collected on the terraces at sites 1 and 2 at the foot of the Pingding Shan have ^{10}Be CRN model ages younger than 19 ka. 90% of these samples were thus deposited after the Last Glacial Maximum (LGM). Moreover, 80% of the model ages (47/58) are younger than 14.5 ka, which demonstrates that the bulk of the terraces that compose the fan complexes of streams S1 and S2, hence the local bajada, formed during the warm post-glacial period of increased run-off that followed the dry glacial age, as found in several other regions of Tibet and central Asia [i.e., *Li et al.*, 2005; *Mériaux et al.*, 2005; *Van der Woerd et al.*, 1998]. A straightforward corollary of this conclusion is that ages >14.5 ka in the data set are likely outliers with pre-depositional exposure that should not be used to constrain the ages of the terraces. Keeping this first-order climatic boundary condition in mind, the CRN data obtained must be interpreted, as is usual, within a framework that takes into account surface processes capable of biasing surface exposure ages toward younger or older values.

[32] Inheritance is the only process that may bias an age population toward apparently older values, implying that the actual age of the samples is younger. For lack of a profile yielding clear exponential decay with decreasing depth, we cannot estimate the average inheritance of surface samples, if any. The fact, however, that several of the best developed terraces contain a small number of samples with ages much older than the bulk implies that such samples have variable inheritance, and thus should be identified as outliers with pre-depositional exposure. Moreover, the two samples collected at 70 and 85 cm depths in T2 at site 1 have ages so young that they suggest inheritance on order of 0.4 to 1.2 ka even on the young average age (∼4.5 ka) of the T2 samples. We conclude that a minimum bias on order of ∼10% toward older ages (no greater than the inherent measurement errors) may exist at both sites, and that the greatest contribution to inheritance is in the outliers, which have been rightfully discarded by the Chauvenet's criterion.

[33] Shielding and erosion are two of the main processes that can bias age populations toward apparently younger values. At both sites 1 and 2, shielding might be thought to have taken place due to transient snow or loess accumulation on the terrace surfaces. Recent work in the Alaskan range, a

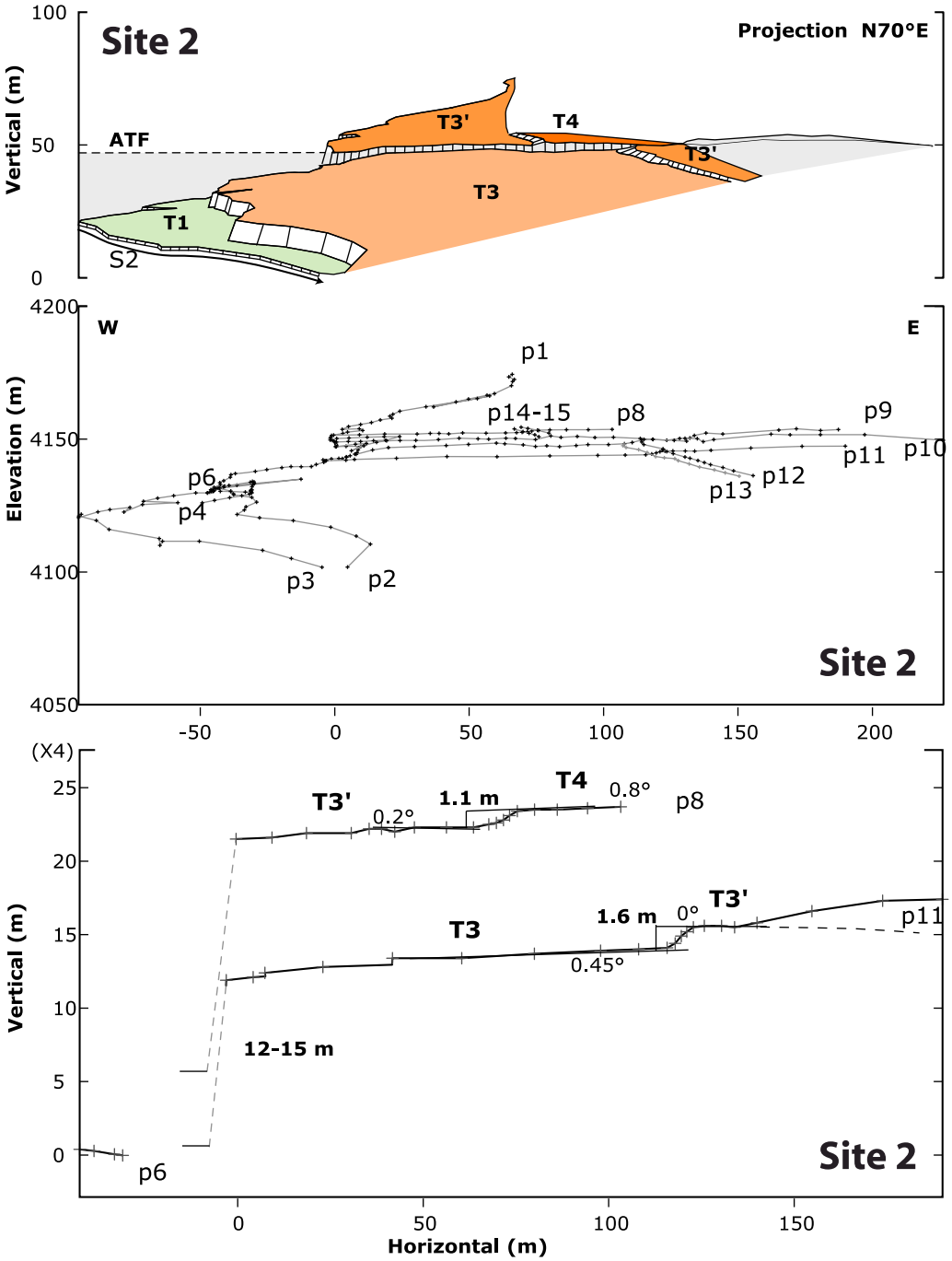

Figure 14. Site 2. Projection on locally N70°-striking plane of total station profiles. (top and middle) Frames showing 1 × 1 scale projected profiles. (bottom) Frame showing projection, with vertical exaggeration of five, of profiles p8, p11, and p6, parallel to fault strike, displaying relative heights of terraces and corresponding risers.

humid region with abundant snowfall, shows that the apparent age younging due to a mean yearly snow cover of ~70 cm over an exposure period of ~10 ka is only on order of 10% [*Mériaux et al.*, 2009]. Here, in the dry continental environment of NE Tibet, on the edge of the Taklamakan desert, it is doubtful that such a correction would reach more than a few percent, and then only during the relatively most humid period of the Early Holocene Optimum (EHO, ~9–6 ka [*Gasse et al.*, 1991]). Thus a younging bias due to snow, if any, would be less than the propagated error on the model ages, and would not even cancel the minimum inheritance bias toward older ages.

[34] We see no trace of potential shielding by loess at either site. Where loess accumulates on terrace surfaces, it usually does so in an uneven manner, becoming tens of cm to even meters thick at places, especially leeward of crests such as those of risers. Vegetation tufts or patches then tend to grow upon loess-mantled areas, preventing subsequent

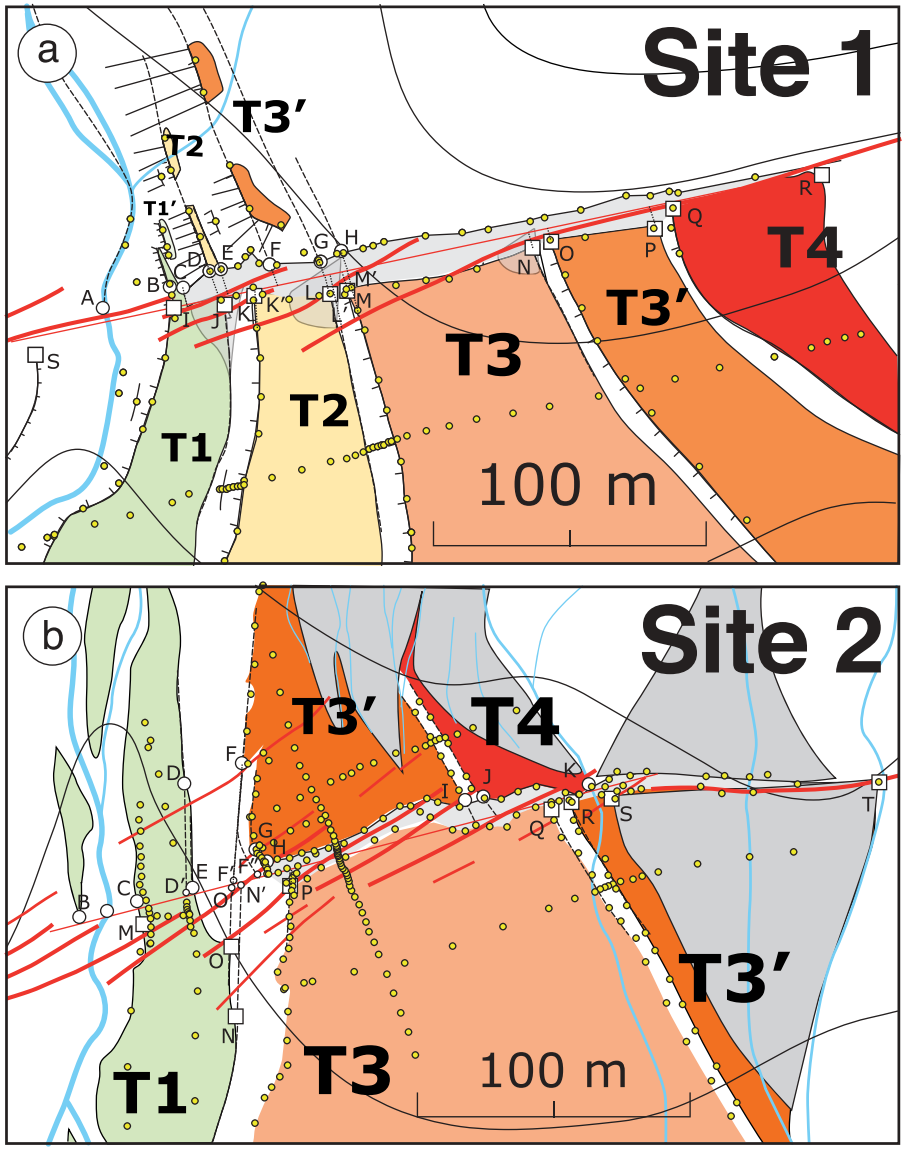

Figure 15. Total-station profiles and high-resolution Quickbird image have been used to define the piercing points of the offset terraces at (a) site 1, (b) site 2. Each piercing point was given a letter of the alphabet (Table 1) and distances between points were measured along an average fault line (thin red line). Same coloring for the different terrace levels as for Figure 6a (site 1) and 6b (site 2). See discussion in text.

erosion of this windblown deposit. As the photographs of Figures 7 and 8 show, the only places where a veneer of silt (wash and/or loess) is visible today is at the foot of the large risers (particularly T2/T1). But such veneers are quite thin (~20 cm) and we avoided sampling the corresponding areas. One might imagine that a loess cover existed in the past on the terraces and was subsequently blown or washed away. But it would have had to have been eliminated completely, with no remnant patch anywhere, a very unlikely scenario. In short, the physiography and aspect of the terraces indicate that shielding by loess at either site cannot have been an important issue at any time during the Holocene. Note that in any case, even at sites where loess accumulation was significant such as near Aksay [*Mériaux et al.*, 2005], we found good agreement between terrace ages constrained by both

Table 1. Terrace Riser Offsets at Site 1 and 2[a]

Terrace Riser	Base (m)	Top (m)
	Site 1	
T1/T0	0 (BI)	0 (BI)
T2/T1	13 (CJ)	15 (DK′)
T3′-T3/T2	38 (EL′)	26–44 (EF-M′)
T4/T3′	122 (GP)	122 (HQ)
	Site 2	
T1/T0	0 (CM)	0 (CM)
T3-T3′/T1	20 (D′N′)	22–40 (D′F′-P)
T3′/T3-T1	110–138 (D′F″-G)	118–127 (F′F″-R)
T4/T3′	>148 (IT)	undefined

[a]Letters refer to piercing point positions defined in Figure 15.

Table 2. Bounds of the Terrace Offsets at Site 1 and 2

Site	Terrace Name	Minimum Offset	Maximum Offset
Site 1	T1	Top of T1/T0 BI 0 m	Base of T2/T1 CJ 13 m
	T2	Top of T2/T1 DK′ 15 m	Base of T3′-T3/T2 EL′ 38 m
	T3	Top of T3/T2 EF-M′ 26–44 m	undefined min EF-N ≪ max GP 94–112 m ≪ 122 m
	T3′	undefined min OF ≪ max GP 101 m ≪ 122 m	Base of T4/T3′ GP 122 m
	T4	Top of T4/T3′ HQ 122 m	undefined >HR >179 m
Site 2	T1	Top of T1/T0 CM 0 m	Base of T3′-T3/T1 D′N′ 20 m
	T2 not present		
	T3	Top of T3/T1 D′F′-P 22–40 m	undefined min D′F″-Q ≪ max IT[a] 110–138 ≪ 148 m
	T3′	undefined min F′F″-R ≪ max IT[a] 118–127 ≪ 148	Base of T4/T3′ >IT[a] >148 m
	T4	Top of T4/T3′ >IT 148 m	undefined

[a]T4 is absent south of the fault and T3′ covered by recent colluvium so that the eastern maximum extension of T3′ south of the fault is ill defined; IT is a minimum.

CRN and ^{14}C dating, provided remnant loess patches were not targeted for sampling.

[35] Surface erosion can also bias CRN model ages toward younger values. Given the rather young age span obtained here at both sites (0.2–14 ka), the effect of erosion should remain limited. An erosion rate of 20 m/Ma (2 cm/ka), for instance, would reduce the actual model age of 4.5 and 7.8 ka old terraces by only 7 and 12%, respectively [see, e.g., *Mériaux et al.*, 2004, Figure 14]. Such a large erosion rate would thus young the terrace surfaces by only ∼10%, an amount smaller than the typical uncertainties of the CRN model ages. Differential erosion, where small particles are removed by wind while larger clasts pile up on the surface to form a depleted desert pavement, would result in a spread toward younger values in CRN model age distributions and thus increase the standard deviation of a given age population. The surface sample population ends up as a mix of samples that received the entire cosmic ray flux since the abandonment of the surface, and of other samples exhumed from shallow depths where they were shielded. Consider a progressive deflation of 10 cm since the abandonment of the T2 terrace surface, whose abandonment age we take to be that of its oldest sample (5.72 ka). Samples exhumed from 10 cm beneath the surface (which would have reached it at a rate of 1.7×10^{-4} cm/yr), would result in only a 4% deviation toward younger model ages. Similarly, a 30 cm deflation of T2 at a rate of 5.2×10^{-4} cm/yr would increase the model age spread by about 10%. While the actual spread of the CRN model age populations on T2 is on average 25%, the fact that the youngest surface sample on T2 (3.8 ka) is almost identical to the youngest depth profile sample (3.2 ka) implies very small amount of deflation, on the order of only a few cm. Finally, it is on the youngest terrace T1, whose surface is least likely to have been affected by deflation that the greatest spread of CRN model ages (88%) is observed. This implies that the dispersion of the CRN model ages on the Holocene terraces at both sites results principally from inheritance and only marginally from deflation. In any event, CRN model age younging by whatever form of erosion on the surfaces of T1-T3′ is unlikely to exceed the propagated errors on such ages.

[36] We thus conclude that, overall, the CRN model ages of the different terrace levels at either site have been modulated principally by the effects of variable inheritance, probably the chief problem in dating Holocene terraces with CRN dating, and of post-depositional contamination of the uppermost terrace treads (T3′, T4) at site 2. The model ages quality varies from terrace to terrace as attested by the MSWQ of the sample clusters. T2, T3 and T3′ are much better dated than T1 (or T4) and each mean cluster age is bracketed by a minimum and maximum age (Table 4). The minimum age of T2 is corrected for inheritance, using the minimum estimate of 820 years derived from the youngest depth sample age. The age of the other terraces are not corrected for inheritance, although the effect of such corrections are discussed where appropriate.

[37] Ultimately, the ages of the different terraces (T4, T3′, T3, T2, and T1) constrain the ages of the cumulative offsets of the respective terrace levels and hence provide independent bounds on the millennial sinistral slip-rate along the Pingding segment of the main strand of the ATF at ∼90.7°E (Table 6, and Figures 15, 17, and 18). Below, we discuss the full range of terrace offsets with the correspondingly large uncertainties, rather than specific model-dependent lower or upper terrace/riser relations (Figure 15). For the ages assigned for each terraces, we used the minimum and maximum CRN model age of each cluster defined using Chauvenet's criterion (Tables 3 and 6).

[38] Deriving slip-rates along strike-slip faults requires a number of assumptions concerning the relationship between the inferred ages of the offset morphological markers. e.g., terrace risers, and the analytically determined ages of the bounding terraces (Figure 17). At the Pingding Shan sites, the offsets considered are those of the terrace levels which are constrained by their upper and lower offset risers [e.g., *Mériaux et al.*, 2005]. A riser cannot be older than the age of the upper surface. Similarly, a riser cannot be younger than the age of the lower bounding surface, and the age of abandonment of that surface defines a minimum age for that riser [e.g., *Mériaux et al.*, 2005] (Figure 17b). Subsequent assumptions regarding the preservation of the riser following its emplacement (i.e., abandonment of the upper level) and preceding the abandonment of the lower level are usually used to derive a rate [e.g., *Tapponnier et al.*, 2001]. If a river is capable of continually refreshing its banks until renewed incision results in terrace abandonment, then the

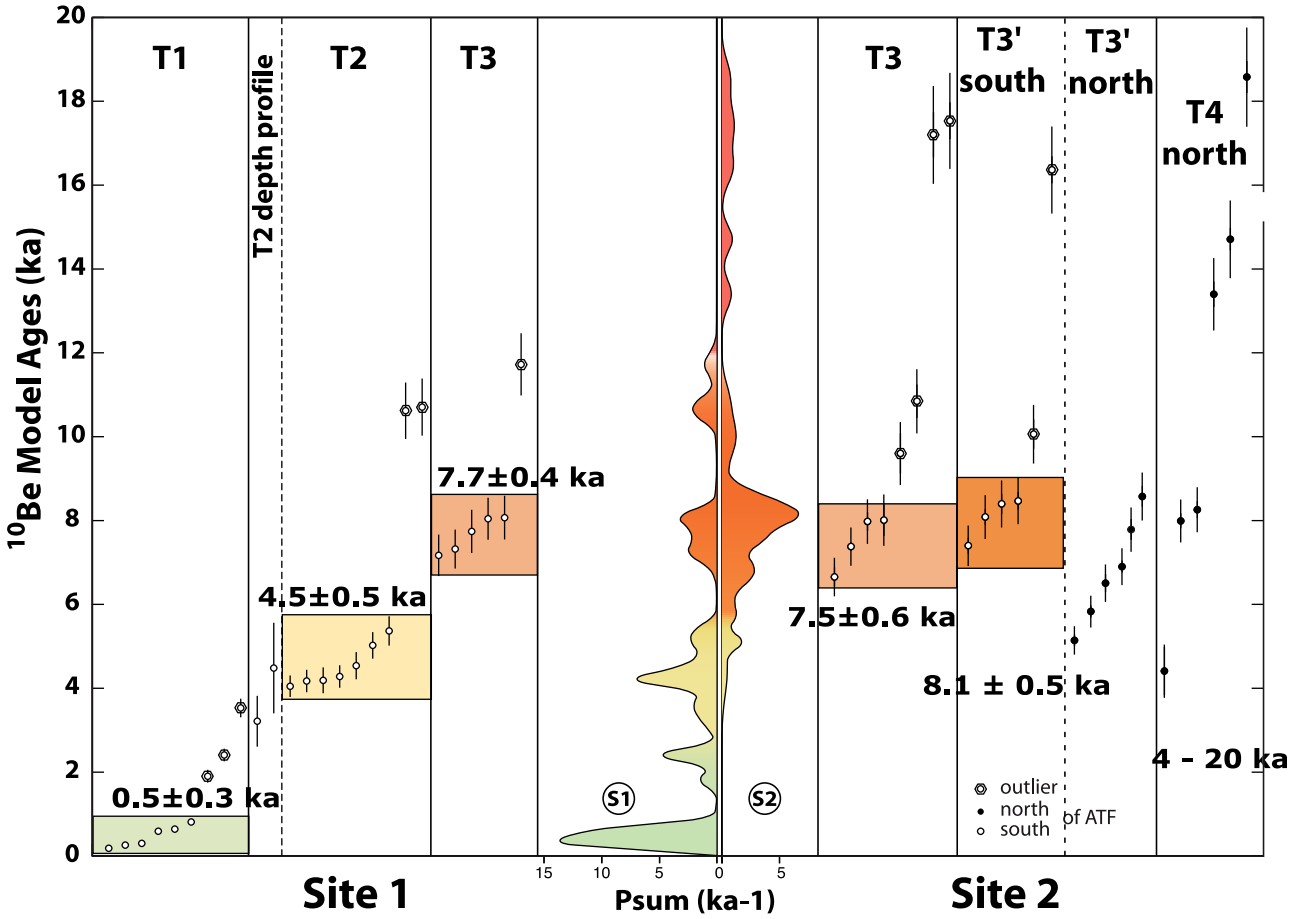

Figure 16. (right) ^{10}Be CRN model ages (≤20 ka) of surface samples collected on T1, T2 and T3 at site 1 (Table 2). Note young clusters on all three terrace levels. (middle) Gaussian age probability distributions at both sites (right, site 1, left, site 2). (left) ^{10}Be CRN model ages (≤20 ka) of surface samples collected onT3, T3′ and T4 at site 2 (Table 4). Note that T3 terraces have similar average ages (7.7 ± 0.4 ka, and 7.5 ± 0.6 ka) at both sites. To improve legibility of age clusters, the plot is restricted to ages ≤20 ka, some data plot off scale (see Tables 2 and 3). The mean age cluster values and outliers are defined using Chauvenet's criterion (Table 3).

association of the riser with the lower terrace age is valid. However, ephemeral rivers may not have sufficient power to continually refresh their banks, and terrace abandonment could be diachronous with some riser displacement accumulated before final abandonment. These effects, which likely depend on river dynamics and the amount of displacement during each earthquake, are difficult to quantify and are also likely dependent of the local timing and synchronization of both fluvial incision as modulated by climate changes and earthquakes. Ultimately, the critical weakness of any morphological analysis to derive slip-rates along strike-slip faults relies on the struggle to date the offset risers. Because, we date at best the various terrace levels, the unambiguous alternative is to associate the offsets of each level - rather than each offset riser – directly with their age estimate (Figure 17c). By definition, dating a riser age with the ages of the bounding terraces is an approximation. Moreover, risers are by essence transient morphological features that erode differently whether upstream or downstream of the strike-slip fault trace and on the right or left bank of the active river bed. Therefore, the age of a terrace riser vary depending on its location with respect to the strike-slip fault trace and the river.

[39] Here, the bounds on the rate are directly established by considering the bounds of the terrace tread offset and their respective age, leading to minimum and maximum values for the rate (Figures 17c and 18). In order to limit the effects of inheritance and post-contamination to our defined cluster age, only the minimum and maximum of the data in each cluster will be considered. In other words, a constant probability between the extreme ages (a_{min}, a_{max}) will be examined rather than a Gaussian age distribution centered on the mean. Similarly, each terrace offset is taken to have an uniform probability between its lower and upper values d_{min} and d_{max}, instead of using any preferred offset value, which might be a source of bias on the resulting rate [*Cowgill*, 2007; *Mériaux et al.*, 2004]. Then, to derive the slip-rates, we calculate rate probability distributions $Pv(v)$ as done previously by [*Daëron et al.*, 2004; *Zechar and Frankel*, 2009] but without assuming any Gaussian distributions on the ages (A) and on the offsets (D).

Table 3. CRN ^{10}Be and ^{26}Al Model Ages at Site 1[a]

Sample	NBe	NAl	Depth[b]	Be Age[c]	Al Age[c]
			T1		
QGQ-18	6.0567 ± 0.0026	0.3708 ± 0.0264	0 (0.98)	0.81 ± 0.08 (0.04)	0.79 ± 0.09 (0.06)
QGQ-19	0.1330 ± 0.0071	0.6881 ± 0.0286	0 (0.98)	1.89 ± 0.20 (0.10)	1.47 ± 0.15 (0.06)
QGQ-20	0.1684 ± 0.0033	1.1089 ± 0.0402	0 (0.98)	2.40 ± 0.22 (0.05)	2.37 ± 0.23 (0.09)
QGQ-21	0.0413 ± 0.0024	0.2677 ± 0.0181	0 (0.98)	0.59 ± 0.06 (0.03)	0.57 ± 0.06 (0.04)
QGQ-22	0.0183 ± 0.0026	0.1173 ± 0.0178	0 (0.98)	0.26 ± 0.04 (0.04)	0.25 ± 0.04 (0.04)
QGQ-23	0.0129 ± 0.0034	0.1021 ± 0.0117	0 (0.98)	0.18 ± 0.05 (0.05)	0.22 ± 0.03 (0.02)
QGQ-24	0.2467 ± 0.0045	1.5111 ± 0.0661	0 (0.98)	3.51 ± 0.33 (0.06)	3.23 ± 0.33 (0.14)
QGQ-25	0.0211 ± 0.0017	0.1575 ± 0.0424	0 (0.98)	0.30 ± 0.04 (0.02)	0.34 ± 0.10 (0.09)
QGQ-26	0.0449 ± 0.0039	0.2755 ± 0.0440	0 (0.98)	0.64 ± 0.08 (0.06)	0.59 ± 0.11 (0.09)
			T2		
QGQ-9	0.7486 ± 0.0153	4.6775 ± 0.1606	0 (0.98)	10.66 ± 0.99 (0.22)	10.00 ± 0.98 (0.34)
QGQ-10	0.2836 ± 0.0055	1.8153 ± 0.0700	0 (0.98)	4.03 ± 0.37 (0.08)	3.87 ± 0.38 (0.15)
QGQ-11	0.3758 ± 0.0095	2.3228 ± 0.1176	0 (0.98)	5.34 ± 0.50 (0.13)	4.95 ± 0.52 (0.25)
QGQ-12	0.2999 ± 0.0054	1.9298 ± 0.1010	0 (0.98)	4.26 ± 0.39 (0.08)	4.11 ± 0.43 (0.22)
QGQ-13	0.3518 ± 0.0071	2.1189 ± 0.0769	0 (0.98)	5.00 ± 0.46 (0.10)	4.52 ± 0.44 (0.16)
QGQ-14	0.3179 ± 0.0122	2.0262 ± 0.0626	0 (0.98)	4.52 ± 0.45 (0.17)	4.32 ± 0.42 (0.13)
QGQ-15	0.2934 ± 0.0126	2.0517 ± 0.1230	0 (0.98)	4.17 ± 0.42 (0.18)	4.38 ± 0.48 (0.26)
QGQ-16	0.2923 ± 0.0064	1.6920 ± 0.0785	0 (0.98)	4.15 ± 0.39 (0.09)	3.61 ± 0.37 (0.17)
QGQ-17	0.7426 ± 0.0145	4.6793 ± 0.2256	0 (0.98)	10.57 ± 0.98 (0.21)	10.01 ± 1.04 (0.48)
			T2 Depth Profile		
QGQ-29	0.1928 ± 0.0061	1.1725 ± 0.0628	85 (0.60)	4.47 ± 1.28 (0.25)	4.09 ± 1.20 (0.39)
QGQ-30	0.1498 ± 0.0036	1.0234 ± 0.0425	70 (0.65)	3.21 ± 0.75 (0.13)	3.30 ± 0.78 (0.22)
T3					
QGQ-1	2.2709 ± 0.0366	13.9484 ± 0.4880	0 (0.98)	32.42 ± 2.97 (0.52)	30.04 ± 2.98 (1.05)
QGQ-2	0.5642 ± 0.0093	3.6553 ± 0.1395	0 (0.98)	8.01 ± 0.74 (0.13)	7.79 ± 0.77 (0.30)
QGQ-3	0.5782 ± 0.0136	3.9196 ± 0.1489	0 (0.98)	8.02 ± 0.75 (0.19)	8.16 ± 0.81 (0.31)
QGQ-4	0.5431 ± 0.0156	3.6011 ± 0.1685	0 (0.98)	7.71 ± 0.73 (0.22)	7.67 ± 0.79 (0.36)
QGQ-5	2.2175 ± 0.0514	13.8021 ± 0.5713	0 (0.98)	31.65 ± 2.94 (0.73)	29.73 ± 3.02 (1.23)
QGQ-6	0.5031 ± 0.0169	2.9304 ± 0.1152	0 (0.98)	7.14 ± 0.69 (0.24)	6.24 ± 0.62 (0.25)
QGQ-7	0.5136 ± 0.0103	3.1822 ± 0.1066	0 (0.98)	7.29 ± 0.68 (0.15)	6.78 ± 0.66 (0.23)
QGQ-8	0.8394 ± 0.0140	5.1654 ± 0.1702	0 (0.98)	11.65 ± 1.08 (0.23)	10.77 ± 1.05 (0.35)

[a]NBe and NAl are the concentration of atoms, unit: 10^6 atoms/g. Be concentrations are corrected for the revised standard [*Nishiizumi et al.*, 2007].

[b]Depth of samples (cm), the thickness and depth corrections for spallation reactions are in brackets. Corrections are similar to the CRONUS-Earth calculator v2.2 but used the attenuation length of *Farber et al.* [2008], a density of ρ = 2.6 g/cm^3 for the thickness correction of each sample and a density of ρ = 2.2 g/cm^3 for the overburden sediments above the depth samples.

[c]Zero erosion and zero inferitance model ages are calculated similarly than the Stone/Lal scaling scheme of *Balco et al.* [2008]. The propagated uncertainties include 9% uncertainty on production rate (CRONUS-Earth calculator v2.2), 2.8% uncertainties for decay constants of 26Al [*Gosse and Phillips*, 2001], 0.87% for decay constants of 10Be [*Korschinek et al.*, 2010], as well as uncertainty of 10% on density and 2.5% on the attenuation length [*Farber et al.*, 2008]. The ages are given in ka. Propagated analytical uncertainties in brackets include error blank, carrier and counting statistics error.

[40] If the offsets (D) and ages (A) are positive variables with density of P_D and P_A, respectively then V = D/A has a density of:

$$P_V(v) = \int_0^\infty aP_D(va)P_A(a)da \tag{2}$$

Let's assume that both A and D have uniform distribution over (a_{min}, a_{max}) and (d_{min}, d_{max}), respectively, where $\Delta a = (a_{max} - a_{min})$ and $\Delta d = (d_{max} - d_{min})$. Then, for V > 0

$$P_V(v) = \int_0^\infty 1_{a_{min}<a<a_{max}} 1_{d_{min}<va<d_{max}} \frac{ada}{\Delta a \Delta d} \tag{3}$$

$$P_V(v) = \int_0^\infty 1_{a_{min}<a<a_{max}} 1_{\frac{d_{min}}{v}<a<\frac{d_{max}}{v}} \frac{ada}{\Delta a \Delta d} \tag{4}$$

where $1_{p<x<q}$ equals 1 if p < x < q and equals 0 otherwise. In general, to have $1_{p<x<q}\ 1_{r<x<s}$ will only equal 1 if x belongs to both intervals, (p, q) and (r, s). That is $1_{p<x<q}1_{r<x<s}$ which of course, require that

$$\max(p, r) > \min(q, r). \tag{5}$$

[41] Therefore, we distinguish the following cases:

[42] (1) If max (a_{min}, d_{min}/v) ≥ min (a_{max}, d_{max}/v), then

$$P_V(v) = 0 \tag{6}$$

[43] (2) If max (a_{min}, d_{min}/v) < min (a_{max}, d_{max}/v), then

$$P_V(v) = \int_{\max(a_{min}, d_{min}/v)}^{\min(a_{max}, d_{max}/v)} \frac{ada}{\Delta d \Delta a} = \frac{\min(a_{max}, d_{max}/v)^2 - \max(a_{min}, d_{min}/v)^2}{2(a_{max} - a_{min})(d_{max} - d_{min})} \tag{7}$$

Table 4. Data Selection of CRN Surface Model Ages Using Chauvenet's Criterion[a]

Number of Samples	Mean	SD	MSWD	Outlier Ages	Cluster Min Age	Cluster Max Age	Comments
Site 1							
T1							
9	1.2	1.2	38.7	3.5			
8	0.9	0.8	31.6	2.4			
7	0.7	0.6	23.0	1.9			
6 (3)	**0.5**	**0.3**	16.0		**0.13**	**0.89**	**Poorly dated**
T2							
9	5.9	2.7	10.3	10.6, 10.7			
7 (2)	**4.5**	**0.5**	**1.2**		**3.66**	**5.85**	**Well dated**
T3							
8	14.3	11.1	20.6	31.7, 32.4			
6	8.3	1.7	2.8	11.7			
5(3)	**7.7**	**0.4**	**0.3**		**6.45**	**8.77**	**Well dated**
Site 2							
T3							
8	10.7	4.3	10.8	17.1, 17.5			
6	8.4	1.5	3.0	10.8, 9.6			
4(4)	**7.5**	**0.6**	**0.8**		**5.99**	**8.70**	**Fairly dated**
T3′ (D)							
8	14.8	9.9	20.3	33.2, 26.6			
6	9.8	3.3	6.3	16.3, 10.0			
4 (4)	**8.1**	**0.5**	**0.9**		**6.67**	**9.23**	**Fairly dated**
T3′ (U)							
7	10.2	9.2	15.2	30.9			
6	6.8	1.3	3.8	0	4.64	9.35	**Poorly dated**
T3′(U+D)							
15	12.7	9.5	19.7	26.6, 30.9, 33.2			
12	8.3	2.9	7.3	16.3			
11	7.5	1.4	4.3	10.0			
6	**8.1**	**0.5**	**0.4**	**5.1, 5.8, 6.5, 6.9**	**6.67**	**9.35**	**Fairly dated**
T4							
7	13.5	7.7	26.6	27.2			
6	11.2	5.2	21.1	4.4, 18.5			
4(3)	11.1	3.5	10.4		7.22	16.00	**Poorly dated**

[a]For each iteration, the mean, standard deviation of the population and the mean squared weighted deviation (MSWD) are indicated. In bold are the data of the final iteration of the criterion. Note that the lower the MSWD and the number of outliers (§) are, the better the surface is dated. Most surfaces tend to have a defined cluster of model ages lower than the initial mean, implying that the chief issue with this data set is a problem of inheritance. However, two surfaces (T3′, T4) also have post-surface contamination evidences. The relative age of the different level (i.e., higher = older, lower = younger) also add to the confidence in the outlier selection.

The normalized rate probability distribution Pv(v) of each offset terraces are presented in Table 6 and Figures 18a and 18b.

[44] Overall, the whole set of data gives rates that range from 0 to 75 mm/yr (Table 6). At both sites, the smaller offset terraces T1 have the wider rate probability distributions ranging between 0 and rates >45 mm/yr, when the larger offset terraces T3′ have narrower rate distributions, ranging from ~11 to 20 mm/yr (Table 6). The T3 offset terraces yield slip-rates ranging from ~3 to 20 mm/yr, while the offset terrace T2 yield slip-rates ranging from ~3 to 12 mm/yr.

[45] Assuming that measurements (offsets and ages) derived from each terrace are independent, the long-term rate at the Pingding Shan can be found by calculating the joint rate distribution [*Rohatgi*, 1976], defined as:

$$P_{V_i V_{i+1} \ldots V_n}(v_i, v_{i+1}, \ldots v_n) = \prod_{i=1}^{n} P_{V_i}(v_i) \quad (8)$$

where $Pv_i(v_i)$ is the normalized rate distribution for the ith terrace and n is the number of terraces. This approach is similar to *Daëron et al.* [2004].

[46] When calculating the joint rate distribution at the Pindging Shan, we do not integrate the rate distributions derived from the lower terrace T1 at both sites, as these are clearly inconclusive. Similarly, we also do not include the rate derived for T3′ at site 1, as that surface is only dated at site 2. Only the rate distributions of the independent dated offset terraces are used to derive the rate at the Pingding Shan (Table 6). Overall, the joint rate distribution for all independent offset terraces at both sites yield a product of probability converging to a rate of 13.9 ± 1,1 mm/yr at the 95% confidence level (Figure 18c).

[47] As can be seen in Figure 18b, the rates derived for T2 barely overlap the rates derived for the older terraces (T3, T3′). Excluding the terrace T2 data to derive the joint slip-rate gives a rate of 15.3 ± 2.3 mm/yr (Figure 18c). This apparent discrepancy in slip-rates may have various explanations: 1) the long-term slip-rate may not be uniform over the different time intervals of terrace formation and abandonment, 2) the CRN model ages determined for the different terraces may be biased toward older ages (inheritance) or toward younger ages (erosion, post-contamination), 3) the offset bounds may be biased due to partial or total erosion of the terrace treads north and south of the fault trace, 4) the offset may be biased in particular for the youngest terraces if the fault is late in its seismic cycle and the next earthquake overdue. Some of these effects have been already discussed above, in particular, the offset measurements, which were maximized between minimum and maximum

Table 5. CRN ^{10}Be Model Ages at Site 2[a]

Sample	NBe	Depth[b]	Be Age[c]
	T3(Downstream)		
QGQ00–28	0.5559 ± 0.0158	0 (0.98)	7.94 ± 0.23 (0.75)
QGQ00–29	0.7450 ± 0.0274	0 (0.96)	10.80 ± 0.40 (1.06)
QGQ00–30	0.5589 ± 0.0263	0 (0.98)	7.98 ± 0.38 (0.82)
QGQ00–31	0.5152 ± 0.0072	0 (0.98)	7.35 ± 0.10 (0.67)
QGQ00–33	0.4648 ± 0.0158	0 (0.98)	6.63 ± 0.22 (0.64)
QGQ00–34	0.6702 ± 0.0334	0 (0.98)	9.56 ± 0.48 (0.99)
QGQ00–35	1.2164 ± 0.0305	0 (0.98)	17.45 ± 0.44 (1.64)
QGQ00–36	1.1915 ± 0.0371	0 (0.98)	17.12 ± 0.53 (1.64)
	T3′(Upstream)		
QGQ00–1	0.3608 ± 0.0097	0 (0.98)	5.12 ± 0.14 (0.48)
QGQ00–2	0.5969 ± 0.0172	0 (0.97)	8.54 ± 0.25 (0.81)
QGQ00–3	0.5465 ± 0.0173	0 (0.98)	7.75 ± 0.25 (0.74)
QGQ00–5	0.4015 ± 0.0101	0 (0.96)	5.81 ± 0.15 (0.55)
QGQ00–6	2.1654 ± 0.0511	0 (0.98)	30.87 ± 0.73 (2.88)
QGQ00–8	0.4568 ± 0.0152	0 (0.98)	6.48 ± 0.22 (0.63)
QGQ00–9	0.4689 ± 0.0098	0 (0.95)	6.88 ± 0.14 (0.64)
	T3′(Downstream)		
QGQ00–18	0.5760 ± 0.0143	0 (0.96)	8.43 ± 0.21 (0.79)
QGQ00–19	2.3265 ± 0.0755	0 (0.99)	33.24 ± 1.08 (3.18)
QGQ00–20	0.5107 ± 0.0131	0 (0.97)	7.37 ± 0.19 (0.69)
QGQ00–21	0.7046 ± 0.0246	0 (0.99)	10.01 ± 0.35 (0.97)
QGQ00–22	1.1536 ± 0.0228	0 (0.99)	16.27 ± 0.32 (1.51)
QGQ00–24	1.8395 ± 0.0336	0 (0.97)	26.64 ± 0.49 (2.45)
QGQ00–25	0.5674 ± 0.0133	0 (0.99)	8.05 ± 0.19 (0.75)
QGQ00–27	0.5821 ± 0.0168	0 (0.97)	8.36 ± 0.24 (0.80)
	T4(Upstream)		
QGQ00–10	1.9158 ± 0.0349	0 (0.99)	27.15 ± 0.49 (2.50)
QGQ00–12	0.9294 ± 0.0211	0 (0.97)	13.34 ± 0.30 (1.24)
QGQ00–13	0.5397 ± 0.0119	0 (0.94)	7.96 ± 0.18 (0.74)
QGQ00–14	0.3116 ± 0.0407	0 (0.99)	4.39 ± 0.57 (0.70)
QGQ00–15	1.0136 ± 0.0187	0 (0.96)	14.65 ± 0.27 (1.35)
QGQ00–16	1.2978 ± 0.0267	0 (0.98)	18.49 ± 0.38 (1.71)
QGQ00–17	0.5795 ± 0.0143	0 (0.98)	8.22 ± 0.20 (0.77)

[a]NBe are the concentration of atoms, unit: 10^6 atoms/g. Be concentrations are corrected for the revised standard [*Nishizumii et al.*, 2007].

[b]Depth of samples (cm), the thickness and depth corrections for spallation reactions are in brackets. Corrections are similar to the CRONUS-Earth calculator v2.2 but used the attenuation length of *Farber et al.* [2008], a density of ρ = 2.6 g/cm^3 for the thickness correction of each sample and a density of ρ = 2.2 g/cm^3 for the overburden sediments above the depth samples.

[c]Zero erosion and zero inheritance model ages are calculated similarly than the Stone/Lal scaling scheme of *Balco et al.* [2008]. The propagated uncertainties include 9% uncertainty on production rate (CRONUS-Earth calculator v2.2), 0.87% for decay constants of 10Be [*Korschinek et al.*, 2010], as well as uncertainty of 10% on density and 2.5% on the attenuation length [*Farber et al.*, 2008]. The ages are given in ka. Propagated analytical uncertainties in brackets include error blank, carrier and counting statistics error.

bounds. Although we cannot exclude that the rate has changed over the time interval of terrace formation, i.e., from 7.5 ka to 4.5 ka, much more data would be needed to confirm this hypothesis. The two other effects may be tested and their implications for the slip-rates are detailed below.

[48] First, we consider the effect of inheritance on the age of the terraces. As discussed before, subsurface samples in the T2 terrace seem to indicate that the surface samples contain an inherited component. Taking the minimum inheritance of 820 yrs derived from the T2 surface and sub-surface samples and applying it to all terraces above T1 results in improved convergence of the data with a resulting slip-rate of 16.5 ± 2.5 mm/yr at the 95% confidence level (Figure S4a). The effects of inheritance clearly decrease with time and become negligible as supported by comparison with results derived for T2 and the higher terraces (T3 and T3′).

[49] Next, we consider a possible slip-deficit along the PDSF. As discussed by previous workers, the average co-seismic displacement along the Pingding Shan segment may reach about 7 m [*Washburn et al.*, 2001]. On the other hand, no recent mole tracks can be seen on the lower T1 terraces at both sites, indicating that an event may be overdue along this segment of the Altyn Tagh Fault. When correcting all the offsets measured by 7 m, the probability distributions are better reconciled with a resulting slip-rate of 15.3 ± 1.8 mm/yr (Figure S4b).

[50] Finally, correcting for both effects - inheritance and slip-deficit - leads to an average rate of 17.5 ± 2.7 mm/yr (Figure S4c). Clearly, addressing the time variability of the rate at these sites would require to better estimate the inheritance at both sites on each level and the co-seismic displacements that may vary from site to site, together with the timing of past events along the Pingding segment of the Altyn Tagh Fault. Although, the inheritance has been roughly estimated on T2 at site 1, establishing whether or not the inheritance remains relatively constant over time is required to refine the CRN model ages. Overall, all the joint rates obtained range from 13 to 18 mm/yr. For now, we will carry forward the long-term slip-rate of 13.9 ± 1.1 mm/yr, defined at 95% confidence level, estimated using all 5 independent terraces (Table 6, Figure 18c).

6. Summary and Discussion

[51] As at the other studies along the Altyn Tagh Fault [*Gold et al.*, 2009, 2011; *Mériaux et al.*, 2004, 2005], the sinistral offsets and terrace ages measured near the eastern extremity of the Pingding range document the kinematic behavior of the main strand of the fault principally during the Holocene (Figure 18). At both sites along the PDSF (Figure 3), the ranges of Holocene sinistral offsets and terrace emplacement ages we obtain are similar to those found along the Aksay segment of the fault [*Mériaux et al.*, 2005], even though the sample population collected is somewhat smaller here. The similarity of average of the ages of T3 samples at both sites here (7.7 ± 0.4 ka and 7.5 ± 0.6 ka), with T2 samples at the Aksay-Banguoba sites (6.5 ± 0.9 ka, with a maximum age distribution at 7.2 ka [*Mériaux et al.*, 2005]), T2 samples at the Cherchen He site (7.3 ± 2.2 ka [*Mériaux et al.*, 2004]), of T2 the Tuzidun site (6.0 ± 0.8 ka [*Gold et al.*, 2009] and T2 at Kelutelage (6.0 ± 2.1 ka) and at Yukuang (6.4 ± 0.1 ka) [*Gold et al.*, 2011]), likely records the imprint of a regionally coeval climatic event along the northern margin of the Tibet plateau, probably a strong pluvial at the end of the warm and humid Early Holocene Optimum [*Gasse et al.*, 1991]. The age of T2 here (4.5 ± 0.5 ka) is about 2 ka older than that of T1 at Aksay (∼2 ka), implying perhaps that, in the absence of strong, regional climatic forcing, river discharge in the latter part of the Holocene was influenced by local weather and catchment location. Note for instance that S1 and S2 are on the south flank of the Pingding Shan while sites along the Aksay segment of the fault lie north of the Dangjin Shankou range. When added to the increasing database provided by similar morphochronologic studies [*Cowgill et al.*, 2009; *Gold et al.*, 2009, 2011; *Harkins and Kirby*, 2008; *Kirby et al.*, 2007;

Table 6. Slip-Rate Estimates Derived From the Rate Distributions Pv

	Offsets		Model Ages[a]		Rates[b]		Bounds of Rates[c]
	Dmin (m)	Dmax (m)	Amin (ka)	Amax (ka)	Vmin (mm/yr)	Vmax (mm/yr)	(mm/yr)
				Site 1			
T1[$]	0	13	0.15	0.89	0	48.9	-
T2	15	38	2.46	5.85	2.8	11.8	2.6–15.4
T3	26	122	6.45	8.77	3.3	16.2	3.0–18.9
T3′[d]	101	122	6.67	9.35	11.3	17.1	10.9–18.2
				Site 2			
T1[d]	0	20	0.15	0.89	0	75.3	-
T3	22	148	5.99	8.7	2.9	20.7	2.6–20.7
T3′	118	148	6.67	9.35	13.2	20.6	12.7–22.1
Joint rate distribution (**13.9 ± 1.1 mm/yr**)					**12.8**	**14.9**	**12.7–15.4**
Joint rate distribution without T2 (**15.3 ± 2.3 mm/yr**)					**13.0**	**17.6**	**12.7–18.9**

[a]Minimum and maximum ages are the bounds of the cluster of the surfaces sample (see Table 3), apart from the minimum age of T2, which is the youngest sample at depth.
[b]Defined at the 95% confidence level.
[c]Outside this interval, the rate probability Pv is null.
[d]Terrace not included to derive the joint rate distribution (see text for details).

Lasserre et al., 2002, 1999; *Li et al.*, 2005; *Mériaux et al.*, 2004, 2005; *Van der Woerd et al.*, 2001, 1998, 2000, 2002b], the Pingding results confirm that most of the abandoned river terraces now lying 10–20 m above present-day river beds in Northern Tibet, and probably also in adjacent regions of central Asia, were emplaced during the pluvial periods that followed deglaciation, as anticipated in earlier work [*Avouac et al.*, 1993b; *Meyer et al.*, 1996, 1998; *Peltzer et al.*, 1989, 1988].

[52] Unlike those of terraces studied near Aksay [*Mériaux et al.*, 2005] and Tura [*Gold et al.*, 2011; *Mériaux et al.*, 2004], the CRN model ages found here are not corroborated by independent ^{14}C dating of subsurface organic material. But the good correlation between such ages here and at these other two localities, as well as their coevality with well-established paleoclimatic patterns in the northern hemisphere, imply that, as elsewhere along the Altyn Tagh and Kunlun Faults, our CRN dating is not significantly biased by either erosion, burial, inheritance or post-abandonment contamination. If anything, the most serious source of error in assessing the ages of T2 to T4 at sites 1 and 2 is inheritance, as suggested by the results of the depth profile samples and by the systematic presence of older outliers in each terrace's sample population. In that case, the terrace emplacement ages might in fact be younger than we infer, and therefore, the slip-rate of 13.9 ± 1.1 mm/yr is unlikely to be overestimated.

[53] The main Pingding strand slip-rate we find is consistent with that obtained using the same technique along the western Aksay segment of the North ATF (17.8 ± 3.6 mm/yr) [*Mériaux et al.*, 2005]. It is also consistent with the lower bound of the rate found to the west along the Tura segment of the ATF (18.4 mm/yr [*Mériaux et al.*, 2004]) and in agreement with the higher bound of the reinterpreted rate at Cherchen [*Cowgill*, 2007], at Tuzidun (8–17 mm/yr [*Gold et al.*, 2009]), at Kelutelage (8.1–13 mm/yr [*Gold et al.*, 2011]), at Yukuang (2.4–14.1 mm/yr [*Gold et al.*, 2011]), at Keke Quiapu at 88.12°E (1.9–15 mm/yr [*Gold et al.*, 2009, 2011]) and at Yuemake (9–14 mm/yr [*Cowgill et al.*, 2009]). Our new rate of the eastern Altyn Tagh Fault along the Pingding strand provides additional evidence that the fault moves at rate of 13–20 mm/yr in its central and eastern part and supports the view of a northeastward decrease of the sinistral slip-rate along the fault (Figure 1).

[54] The rate obtained here is different, however, from rates inferred previously or estimated at adjacent localities with other techniques. To the east and west of Pingding Shan, paleo-earthquake sequences uncovered by trenching [*Washburn et al.*, 2001] and two epochs campaign GPS results [*Bendick et al.*, 2000; *Wallace et al.*, 2004] have been interpreted to indicate a smaller rate than that we find (9 ± 4 mm/yr, $\pm 2\sigma$). The upper bound of that rate (14 mm/yr) overlaps, however, with the minimum bound derived from this study. The apparent disparity between this short-term, decadal slip-rate and our long-term, early Holocene estimate (6–9 ka) is made worse by the fact that the GPS profile surveys of 1994 and 1998, and the two trenching sites (Kulesayi and Xorkol) cross or target the ATF where the geometry of its trace is somewhat simpler (Figure 2). Hence, the slip-rate west and east of the Pingding ranges push-up should be greater than along the Pingding main strand, because the existence of several other minor active fault splays at the longitude of site 1 (95.6°E, Figure 2) ought to add a few mm/yr of slip to the 13.9 ± 1.1 mm/yr we find. Therefore, as at Aksay or Tura on the ATF [*Mériaux et al.*, 2004, 2005], along the Karakorum Fault in western Tibet [*Chevalier et al.*, 2005] or along the Garlock, Owens valley and southern San Andreas faults of California [*Lee et al.*, 2001; *McGill and Sieh*, 1993; *Peltzer et al.*, 2001], it is possible that the factor of about 1.5–2 discrepancy observed reflects a genuine difference between multimillenial and decadal or centennial slip rates, due to transient strain variations on time-scales shorter or on order of the length of the seismic cycle (300 to 1400 years [*Washburn et al.*, 2001]).

[55] Alternatively, the discrepancy may not be real, but merely a consequence of bias or uncertainty in the results of techniques used in this area for the first time. It could be argued, for instance, that only the minimum slip-rates we obtain should be trusted, even though the clear field relationships observed and the conservative hypotheses upon which such minimum values are based make this unlikely. One might also ask whether the preliminary conclusions of the two other studies east and west of the Pingding Shan are not somehow flawed. The Huatugou-Ruoqiang GPS profile

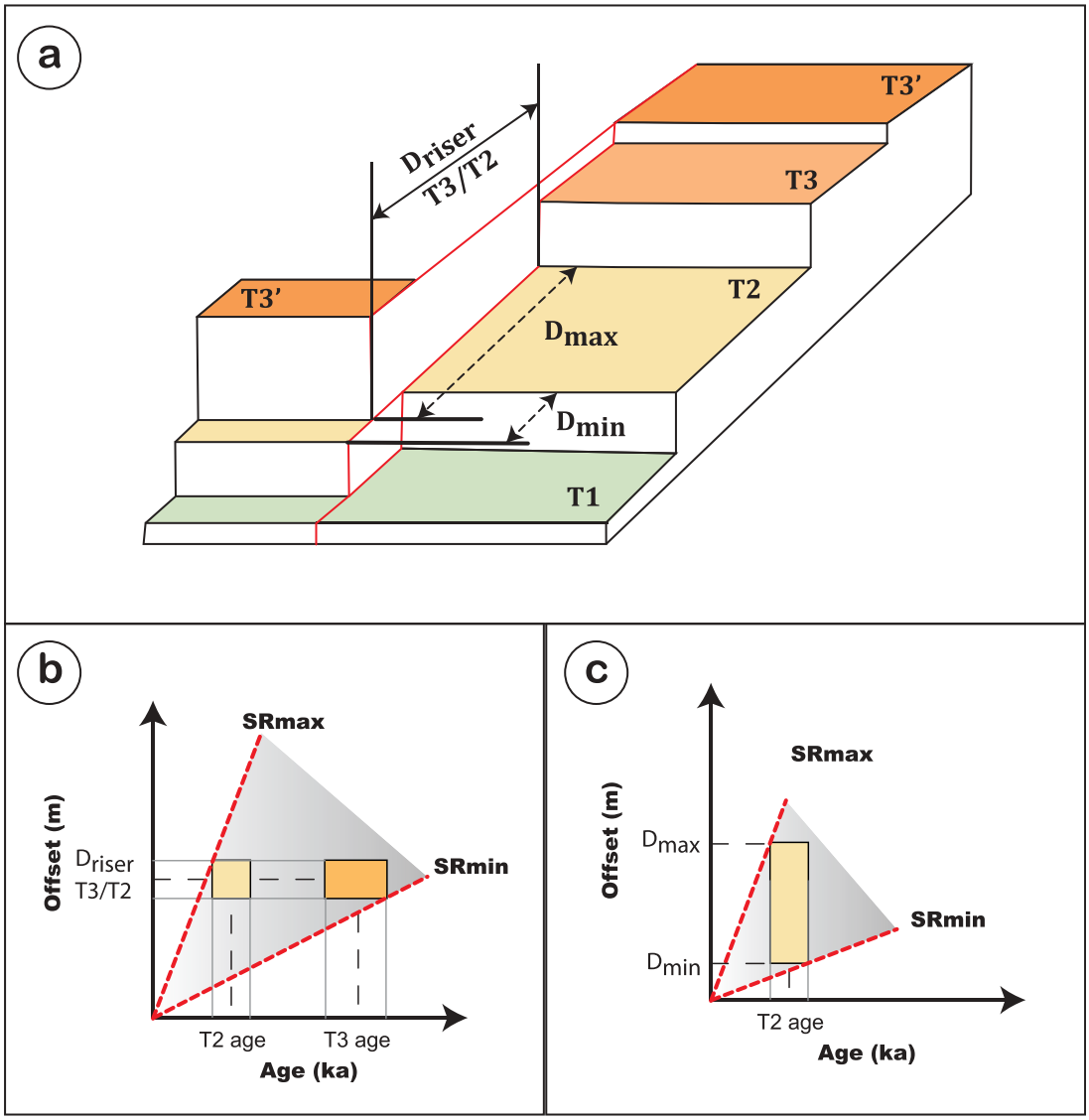

Figure 17. (a) Schematic 3D bloc diagram of terraces setting at site 1. D_{riser} is the offset of the T3/T2 riser, which may have accumulated after abandonment of T2 or after abandonment of T3. If the age of terrace thread T2 is considered, the extreme bounds of its offset range from D_{min} to D_{max}. (b) Slip-rate determination considering the uncertainty in the T3/T2 riser age. Bounds of riser age are the ages of the lower (T2) and upper terrace (T3) from which maximum and minimum rates, respectively, are derived. (c) Slip-rate determination considering the uncertainty in offset accumulation after abandonment of a given terrace. Bounds of the T2 terrace offset are the offsets of its upper T3/**T2** and lower **T2**/T1 risers.

(Figure 1) was surveyed three times (1994, 1998 and 2002), and the pattern of displacements and elastic strain derived from differentiating the two measurement epochs is not that typically observed across a locked strike-slip fault [*Bendick et al.*, 2000; *Wallace et al.*, 2004]. Displacements recorded by GPS appear to be smaller far from the fault than closer to it, similar to GPS profiles across the Haiyuan Fault in Gansu province [*Lasserre*, 2000]. Moreover the GPS displacement of 19.5 mm/yr at PAXI [*Bendick et al.*, 2000], a station located on Precambrian basement north of the ATF, was discarded by the authors on the basis of statistics only (too large), rather than on instrumental error. The first-cut interpretation of *Bendick et al.* [2000] was altered by the results of the third survey across the ATF [*Wallace et al.*, 2004], in part because the data of the latter study was affected by regional deformation resulting from the two large earthquakes that occurred on the Kunlun Fault, south of the ATF, between the last two surveys [e.g., *Peltzer et al.*, 1999; *Van der Woerd et al.*, 2002a], as acknowledged by the authors. Moreover, several of the original benchmarks were lost, and new ones, implanted in 1998 and re-measured for the first time in 2002, hardly helped clarify the overall picture.

[56] Other types of uncertainties probably bias the trenching studies performed by *Washburn et al.* [2001]. Two-dimensional trenching is usually not the best technique to determine slip-rates along strike-slip faults because only subordinate vertical throw, useful in identifying paleo-earthquakes, is visible for a given event on vertical cuts

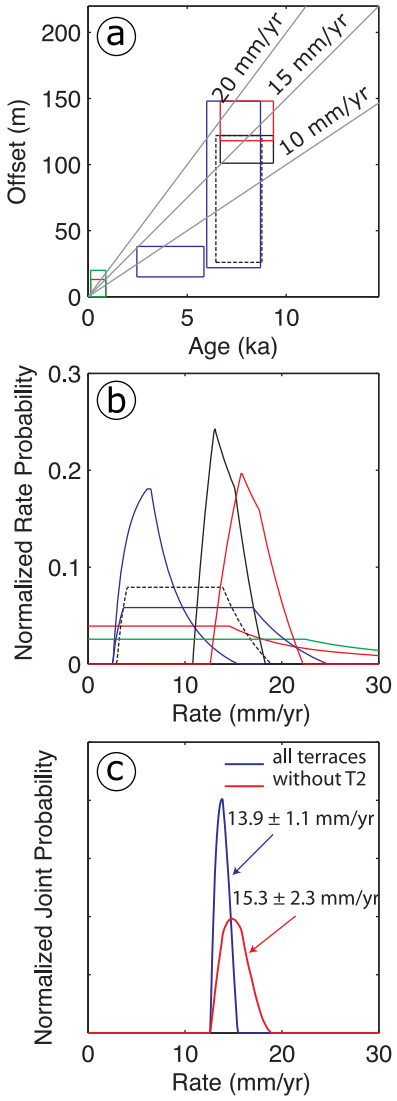

Figure 18. Slip-rate estimates for the 7 offset terraces along main Pingding Shan segment of ATF. (a) Boxes show ranges of values considered equally probable for the 7 independent markers dated (Table 5). (b) Curves are the normalized rate probability distribution, Pv(V), for each marker. (c) Curves correspond to the resulting rates, product of the normalized Pv(V), with all the makers in red and without T2 in blue. The resulting probability distribution with T2 (in red) is multiplied by 1000 for visibility. All rates, Vmin and Vmax, are defined at $\pm 2\sigma$ (Table 4).

across the fault. Event dating in the trenches dug at Kulesayi and Xorkol was based on four ^{14}C dates, a number that would be considered insufficient in most places. The best single-event offsets documented by *Washburn et al.* [2001] were measured far from the trenches in which the paleoseismological records were obtained. In the west, the Most Recent Event offset preferred by the authors is 5.5 m, while *Molnar et al.* [1987b, 1987a] found minimum offsets of ~10 m close to the Kulesayi trench. Finally, the interpretation of the three best trenches dug across the fault remains ambiguous. As acknowledged by the authors, the 1.5 m-deep Kulesayi trench may be interpreted to yield a record of two large earthquakes since 1260 AD. If one assumed the 10 m coseismic-slip value found by *Molnar et al.* [1987b, 1987a] closest to this trench, rather than the 5.5 m value measured much farther east, to be characteristic, then the occurrence of 20 m slip in two events since the 13th century AD would be consistent with a centennial slip-rate >25 mm/yr. Near Xorkol lake, east of Pingding Shan, the fault trace splays into several parallel strands in the area where trenching was performed. Although *Washburn et al.* [2001] conclude that subsurface evidence there is best explained by 2–3 large earthquakes in the last 2.4–3 ka, our field inspection of the fault trace, whose splays preserve free-faced scarps, and examination of the trench logs imply that at least 4 such events are recorded in the upper 2 m of subsurface deposits. Recall that the age control, particularly in layers below those dated at 1270–1305 years AD, is minimal, and the event-displacement (~7 m) used is that determined at Gobiling more than 30 km to the west. If 28 m of slip, resulting from 4 earthquakes, had occurred in 2400 years, the minimum millennial slip-rate on the Xorkol segment of the Altyn Tagh Fault east of the Pingding Shan would be on order of 12 mm/yr. Though this value is not significantly different from the minimum we obtain at Pingding Shan, the fact that there is clear distributed faulting near Xorkol and insufficient age control on the deep events leaves open the possibility of a faster rate.

[57] In summary, more accurate dating of surface and subsurface deposits, as well as precise measurements of single and multiple event offsets across dated horizons at more sites than those targeted so far will be necessary to determine whether the paleoseismological record is more consistent with the morphochronological rates derived from CRN dating over thousands and tens of thousands of years than with the GPS rates, should they be validated by future campaigns.

[58] Considering the uncertainties associated with the other existing data sets, we conclude that neither the displacement of PAXI relative to Mangnai nor the shallowest trenching results are incompatible with a slip-rate greater than ~14 mm/yr between 89°E and 91°E. Such a rate would be consistent with the ~15 mm/yr early Holocene slip-rate found on the main Pingding strand of the ATF if allowance is made for a few millimeters of slip on secondary active splays of the fault system north and south of that strand. A rate on order of 1.7 cm/yr at 90°E would be in keeping with the northeastward decrease of the sinistral slip-rate documented at several sites between Tura and Shibaocheng [*Mériaux et al.*, 2004, 2005; *Meyer et al.*, 1996]. Finally, there may also be no blatant incompatibility either between a sinistral ATF slip-rate of that order at this longitude and the broad-base GPS data set now available at the scale of the entire collision zone. Relative to Siberia, the few velocity vectors measured in central, SE and NW Tibet, north of the Zangbo suture, reach or exceed 2 cm/yr, while several points in the eastern Tarim and Gobi close to the edge of Tibet show negligible movement, within error [e.g., *Wang et al.*, 2001]. Since such vectors are oriented NNE to NE, they imply that ~2 cm/yr of convergence must be absorbed between central Tibet and the eastern Tarim. And north of 33°N, between N83° and N90°E, there is no large active fault other than the ATF with the appropriate orientation and kinematics to take up such shortening. Thus, barring deformation that would not manifest itself by shallow crustal faulting, the central Altyn

Tagh Fault should accommodate a major fraction of the 2 cm/yr convergence between central Tibet and the Tarim, acting as a real plate boundary between the two.

[59] **Acknowledgments.** Sample processing and dating were performed under the auspices of the U.S. Department of Energy, at the University of California Lawrence Livermore National Laboratory, under contract W-7405-Eng-48 and under the sponsorship of the Laboratory Directed Research and Development program (00-ERI-009). We benefited from 4 years of financial and logistical support from Institut National des Sciences de l'Univers, Centre National de la Recherche Scientifique (Paris, France) through programs IDYL and IT and from the China Seismological Bureau and the Ministry of Lands and Resources (Beijing, China). High-resolution Quickbird image was acquired in the frame of project "Spatial paleoseismology" from Programme National de Télédetection Spatiale of INSU-CNRS, France. We thank G.C.P. King and G. Peltzer for thoughtful comments on early versions of the manuscript. A.S.M. would like to thank Catherine Mériaux, Kais Hamza, and Mathieu Daëron for their help with the rate probability distribution calculations. Anne-Claire Morillon provided invaluable help in digitizing the topographic maps of the Pingding Shan area. The reviews of J. Gosse and E. Cowgill helped improve an earlier manuscript. This is Lawrence Livermore National Laboratory report LLNL-JRNL-566181.

References

Avouac, J. P., P. Tapponnier, M. Bai, H. You, and G. Wang (1993), Active thrusting and folding along the northern Tien-Shan and Late Cenozoic rotation of the Tarim relative to Dzungaria and Kazakhstan, *J. Geophys. Res.*, *98*(B4), 6755–6804, doi:10.1029/92JB01963.

Balco, G., J. O. Stone, N. A. Lifton, and T. J. Dunai (2008), A complete and easily accessible means of calculating surface exposure ages or erosion rates from ^{10}Be and ^{26}Al measurements, *Quat. Geochronol.*, *3*(3), 174–195, doi:10.1016/j.quageo.2007.12.001.

Bendick, R., R. Bilham, J. Freymueller, K. Larson, and G. H. Yin (2000), Geodetic evidence for a low slip rate in the Altyn Tagh fault system, *Nature*, *404*(6773), 69–72, doi:10.1038/35003555.

Bevington, P. R., and D. K. Robinson (2002), *Data Reduction and Error Analysis for Physical Sciences*, 336 pp., McGraw-Hill, New York, doi:10.1119/1.17439.

Calais, E., L. Dong, M. Wang, Z. Shen, and M. Vergnolle (2006), Continental deformation in Asia from a combined GPS solution, *Geophys. Res. Lett.*, *33*, L24319, doi:10.1029/2006GL028433.

Chevalier, M. L., F. J. Ryerson, P. Tapponnier, R. C. Finkel, J. Van der Woerd, H. B. Li, and Q. Liu (2005), Slip-rate measurements on the Karakorum Fault may imply secular variations in fault motion, *Science*, *307*(5708), 411–414, doi:10.1126/science.1105466.

Chmeleff, J. M., F. von Blanckenburg, K. Kossert, and D. Jakob (2010), Determination of the ^{10}Be half-life by multicollector ICP-MS and liquid scintillation counting, *Nucl. Instrum. Methods Phys. Res., Sect. B*, *268*(2), 192–199, doi:10.1016/j.nimb.2009.09.012.

Cowgill, E. (2007), Impact of riser reconstructions on estimation of secular variation in rates of strike-slip faulting: Revisiting the Cherchen River site along the Altyn Tagh Fault, NW China, *Earth Planet. Sci. Lett.*, *254*(3–4), 239–255, doi:10.1016/j.epsl.2006.09.015.

Cowgill, E., J. R. Arrowsmith, A. Yin, X. F. Wang, and Z. L. Chen (2004a), The Akato Tagh bend along the Altyn Tagh fault, northwest Tibet 2: Active deformation and the importance of transpression and strain hardening within the Altyn Tagh system, *Geol. Soc. Am. Bull.*, *116*(11), 1443–1464, doi:10.1130/B25360.1.

Cowgill, E., A. Yin, J. R. Arrowsmith, W. X. Feng, and S. H. Zhang (2004b), The Akato Tagh bend along the Altyn Tagh fault, northwest Tibet 1: Smoothing by vertical-axis rotation and the effect of topographic stresses on bend-flanking faults, *Geol. Soc. Am. Bull.*, *116*(11), 1423–1442, doi:10.1130/B25359.1.

Cowgill, E., R. D. Gold, C. Xuanhua, W. Xiao-Feng, J. R. Arrowsmith, and J. Southon (2009), Low Quaternary slip rate reconciles geodetic and geologic rates along the Altyn Tagh fault, northwestern Tibet, *Geology*, *37*(7), 647–650, doi:10.1130/G25623A.1.

Daëron, M., L. Benedetti, P. Tapponnier, A. Sursock, and R. C. Finkel (2004), Constraints on the post-25-ka slip rate of the Yammouneh fault (Lebanon) using in situ cosmogenic Cl-36 dating of offset limestone-clast fans, *Earth Planet. Sci. Lett.*, *227*(1–2), 105–119, doi:10.1016/j.epsl.2004.07.014.

Dayem, K. E., G. A. Houseman, and P. Molnar (2009), Localization of shear along a lithospheric strength discontinuity: Application of a continuous deformation model to the boundary between Tibet and the Tarim Basin, *Tectonics*, *28*, TC3002, doi:10.1029/2008TC002264.

Elliott, J. R., J. Biggs, B. Parsons, and T. J. Wright (2008), InSAR slip rate determination on the Altyn Tagh Fault, northern Tibet, in the presence of topographically correlated atmospheric delays, *Geophys. Res. Lett.*, *35*, L12309, doi:10.1029/2008GL033659.

England, P., and G. Houseman (1986), Finite strain calculations of continental deformation: 2. Comparison with the India-Asia collision zone, *J. Geophys. Res.*, *91*(B3), 3664–3676, doi:10.1029/JB091iB03p03664.

England, P., and P. Molnar (1997), Active deformation of Asia: From kinematics to dynamics, *Science*, *278*(5338), 647–650, doi:10.1126/science.278.5338.647.

Farber, D., A. Mériaux, and R. Finkel (2008), Attenuation length for fast nucleon production of ^{10}Be derived from near-surface production profiles, *Earth Planet. Sci. Lett.*, *274*(3–4), 295–300, doi:10.1016/j.epsl.2008.07.015.

Gasse, F., et al. (1991), A 13,000-year climate record from western Tibet, *Nature*, *353*(6346), 742–745, doi:10.1038/353742a0.

Gaudemer, Y., P. Tapponnier, B. Meyer, G. Peltzer, S. M. Guo, Z. T. Chen, H. G. Dai, and I. Cifuentes (1995), Partitioning of crustal slip between linked, active faults in the eastern Qilian Shan, and evidence for a major seismic gap, the Tianzhu Gap, on the western Haiyuan Fault, Gansu (China), *Geophys. J. Int.*, *120*(3), 599–645, doi:10.1111/j.1365-246X.1995.tb01842.x.

Ge, S., G. Shen, R. Wei, Y. Ding, and Y. Wang (1992), *Active Altun fault Zone Monograph*, 319 pp., State Seismol. Bur. of China, Beijing.

Gold, R. D., and E. Cowgill (2011), Deriving fault-slip histories to test for secular variation in slip, with examples from the Kunlun and Awatere faults, *Earth Planet. Sci. Lett.*, *301*(1–2), 52–64, doi:10.1016/j.epsl.2010.10.011.

Gold, R. D., E. Cowgill, J. R. Arrowsmith, J. C. Gosse, X. Chen, and X. F. Wang (2009), Riser diachroneity, lateral erosion, and uncertainty in rates of strike-slip faulting: A case study from Tuzidun along the Altyn Tagh Fault, NW China, *J. Geophys. Res.*, *114*, B04401, doi:10.1029/2008JB005913.

Gold, R. D., E. Cowgill, J. R. Arrowsmith, X. Chen, W. D. Sharp, K. M. Cooper, and X.-F. Wang (2011), Faulted terrace risers place new constraints on the late Quaternary slip rate for the central Altyn Tagh fault, northwest Tibet, *Geol. Soc. Am. Bull.*, *123*(5–6), 958–978, doi:10.1130/B30207.1.

Gosse, J. C., and F. M. Phillips (2001), Terrestrial in situ cosmogenic nuclides: Theory and application, *Quat. Sci. Rev.*, *20*(14), 1475–1560, doi:10.1016/S0277-3791(00)00171-2.

Harkins, N., and E. Kirby (2008), Fluvial terrace riser degradation and determination of slip rates on strike-slip faults: An example from the Kunlun fault, China, *Geophys. Res. Lett.*, *35*, L05406, doi:10.1029/2007GL033073.

Hidy, A. J., J. C. Gosse, J. L. Pederson, J. P. Mattern, and R. C. Finkel (2010), A geologically constrained Monte Carlo approach to modeling exposure ages from profiles of cosmogenic nuclides: An example from Lees Ferry, Arizona, *Geochem. Geophys. Geosyst.*, *11*, Q0AA10, doi:10.1029/2010GC003084.

Hilley, G. E., K. M. Johnson, M. Wang, Z.-K. Shen, and R. Burgmann (2009), Earthquake-cycle deformation and fault slip rates in northern Tibet, *Geology*, *37*(1), 31–34, doi:10.1130/G25157A.1.

Holt, W. E., N. Chamot-Rooke, X. Le Pichon, A. J. Haines, B. Shen-Tu, and J. Ren (2000), Velocity field in Asia inferred from Quaternary fault slip rates and Global Positioning System observations, *J. Geophys. Res.*, *105*(B8), 19,185–19,209, doi:10.1029/2000JB900045.

Jiao, S., Z. Yifu, Y. Shaoxian, A. Changxing, Z. Younian, L. Yaomin, W. Huaida, X. Jian'e, H. Junqing, and G. Tieying (1988), Geological map of Qinghai-Xizang (Tibet) Plateau and adjacent areas, scale: 1/1,500,000, Chengdu Inst. of Geol. Resour., Chin. Acad. of Geol. Sci., Beijing.

Jolivet, R., R. Cattin, N. Chamot-Rooke, C. Lasserre, and G. Peltzer (2008), Thin-plate modeling of interseismic deformation and asymmetry across the Altyn Tagh fault zone, *Geophys. Res. Lett.*, *35*, L02309, doi:10.1029/2007GL031511.

Kirby, E., N. Harkins, E. Wang, X. Shi, C. Fan, and D. Burban (2007), Slip rate gradients along the eastern Kunlun fault, *Tectonics*, *26*, TC2010, doi:10.1029/2006TC002033.

Kohl, C. P., and K. Nishiizumi (1992), Chemical isolation of quartz for measurement of in situ–produced cosmogenic nuclides, *Geochim. Cosmochim. Acta*, *56*(9), 3583–3587, doi:10.1016/0016-7037(92)90401-4.

Korschinek, G., A. Bergmaier, T. Faestermann, U. C. Gerstmann, K. Knie, G. Rugel, A. Wallner, I. Dillmann, G. Dollinger, and C. L. von Gostomski (2010), A new value for the half-life of ^{10}Be by heavy-ion elastic recoil detection and liquid scintillation counting, *Nucl. Instrum. Methods Phys. Res., Sect. B*, *268*(2), 187–191, doi:10.1016/j.nimb.2009.09.020.

Lal, D. (1991), Cosmic-ray labeling of erosion surfaces: In situ nuclide production-rates and erosion models, *Earth Planet. Sci. Lett.*, *104*(2–4), 424–439, doi:10.1016/0012-821X(91)90220-C.

Lasserre, C. (2000), Fonctionnement sismique, cinématique et histoire géologique de la faille d'Haiyuan, PhD thesis, Univ. of Paris VII, Paris.

Lasserre, C., et al. (1999), Postglacial left slip rate and past occurrence of M > = 8 earthquakes on the western Haiyuan fault, Gansu, China, *J. Geophys. Res.*, *104*(B8), 17,633–17,651, doi:10.1029/1998JB900082.

Lasserre, C., Y. Gaudemer, P. Tapponnier, A. S. Meriaux, J. Van der Woerd, D. Y. Yuan, F. J. Ryerson, R. C. Finkel, and M. W. Caffee (2002), Fast late Pleistocene slip rate on the Leng Long Ling segment of the Haiyuan fault, Qinghai, China, *J. Geophys. Res.*, *107*(B11), 2276, doi:10.1029/2000JB000060.

Lee, J., J. Spencer, and L. Owen (2001), Holocene slip rates along the Owens Valley Fault, California: Implications for the recent evolution of the Eastern California Shear Zone, *Geology*, *29*(9), 819–822, doi:10.1130/0091-7613(2001)029<0819:HSRATO>2.0.CO;2.

Li, H. B., J. Van der Woerd, P. Tapponnier, Y. Klinger, X. X. Qi, J. S. Yang, and Y. T. Zhu (2005), Slip rate on the Kunlun fault at Hongshui Gou, and recurrence time of great events comparable to the 14/11/2001, Mw similar to 7.9 Kokoxili earthquake, *Earth Planet. Sci. Lett.*, *237*(1–2), 285–299.

Loveless, J. P., and B. J. Meade (2011), Partitioning of localized and diffuse deformation in the Tibetan Plateau from joint inversions of geologic and geodetic observations, *Earth Planet. Sci. Lett.*, *303*(1–2), 11–24, doi:10.1016/j.epsl.2010.12.014.

Lowell, T. V. (1995), The application of radiocarbon age estimates to the dating of glacial sequences: An example from the Miami Sublobe, Ohio, USA, *Quat. Sci. Rev.*, *14*(1), 85–99, doi:10.1016/0277-3791(94)00113-P.

McGill, S., and K. Sieh (1993), Holocene slip rate of the central Garlock Fault in southeastern Searles Valley, California, *J. Geophys. Res.*, *98*(B8), 14,217–14,231, doi:10.1029/93JB00442.

Meade, B. J. (2007), Present-day kinematics at the India-Asia collision zone, *Geology*, *35*(1), 81–84, doi:10.1130/G22924A.1.

Mériaux, A.-S. (2002), Détermination par datation cosmogénique des variations de la vitesse de glissement sur la faille de l'Atlyn Tagh depuis 100 ka, PhD thesis, Univ. of Paris VII, Paris.

Mériaux, A.-S., F. J. Ryerson, P. Tapponnier, J. Van der Woerd, R. C. Finkel, X. W. Xu, Z. Q. Xu, and M. W. Caffee (2004), Rapid slip along the central Altyn Tagh Fault: Morphochronologic evidence from Cherchen He and Sulamu Tagh, *J. Geophys. Res.*, *109*, B06401, doi:10.1029/2003JB002558.

Mériaux, A.-S., et al. (2005), The Aksay segment of the northern Altyn Tagh fault: Tectonic geomorphology, landscape evolution, and Holocene slip rate, *J. Geophys. Res.*, *110*, B04404, doi:10.1029/2004JB003210.

Mériaux, A.-S., K. Sieh, R. C. Finkel, C. Rubin, M. Taylor, A. J. Meltzner, and F. J. Ryerson (2009), Kinematic behavior of southern Alaska constrained by westward decreasing postglacial slip rates on the Denali Fault, Alaska, *J. Geophys. Res.*, *114*, B03404, doi:10.1029/2007JB005053.

Métivier, F., Y. Gaudemer, P. Tapponnier, and B. Meyer (1998), Northeastward growth of the Tibet plateau deduced from balanced reconstruction of two depositional areas: The Qaidam and Hexi Corridor basins, China, *Tectonics*, *17*(6), 823–842, doi:10.1029/98TC02764.

Meyer, B., P. Tapponnier, Y. Gaudemer, G. Peltzer, S. M. Guo, and Z. T. Chen (1996), Rate of left-lateral movement along the easternmost segment of the Altyn Tagh fault, east of 96 degrees E (China), *Geophys. J. Int.*, *124*(1), 29–44, doi:10.1111/j.1365-246X.1996.tb06350.x.

Meyer, B., P. Tapponnier, L. Bourjot, F. Metivier, Y. Gaudemer, G. Peltzer, G. Shunmin, and C. Zhitai (1998), Crustal thickening in Gansu-Qinghai, lithospheric mantle subduction, and oblique, strike-slip controlled growth of the Tibet plateau, *Geophys. J. Int.*, *135*(1), 1–47, doi:10.1046/j.1365-246X.1998.00567.x.

Molnar, P., B. C. Burchfiel, Z. Y. Zhao, K. Y. Liang, S. J. Wang, and M. M. Huang (1987a), Geologic evolution of northern Tibet: Results of an expedition to Ulugh-Muztagh, *Science*, *235*(4786), 299–305, doi:10.1126/science.235.4786.299.

Molnar, P., B. C. Burchfiel, L. Kuangyi, and Z. Ziyun (1987b), Geomorphic evidence for active faulting in the Altyn Tagh and northern Tibet and qualitative estimates of its contribution to the convergence of India and Eurasia, *Geology*, *15*(3), 249–253, doi:10.1130/0091-7613(1987)15<249:GEFAFI>2.0.CO;2.

Nishiizumi, K., et al. (2007), Absolute calibration of ^{10}Be AMS standards, *Nucl. Instrum. Methods Phys. Res. B*, *258*(2), 403–413.

Peltzer, G., and F. Saucier (1996), Present-day kinematics of Asia derived from geologic fault rates, *J. Geophys. Res.*, *101*(B12), 27,943–27,956, doi:10.1029/96JB02698.

Peltzer, G., P. Tapponnier, Y. Gaudemer, B. Meyer, S. M. Guo, K. L. Yin, Z. T. Chen, and H. G. Dai (1988), Offsets of Late Quaternary morphology, rate of slip, and recurrence of large earthquakes on the Chang Ma Fault (Gansu, China), *J. Geophys. Res.*, *93*(B7), 7793–7812, doi:10.1029/JB093iB07p07793.

Peltzer, G., P. Tapponnier, and R. Armijo (1989), Magnitude of Late Quaternary left-lateral displacements along the north edge of Tibet, *Science*, *246*(4935), 1285–1289, doi:10.1126/science.246.4935.1285.

Peltzer, G., F. Crampe, and G. King (1999), Evidence of nonlinear elasticity of the crust from the Mw7.6 Manyi (Tibet) earthquake, *Science*, *286*(5438), 272–276, doi:10.1126/science.286.5438.272.

Peltzer, G., F. Crampe, S. Hensley, and P. Rosen (2001), Transient strain accumulation and fault interaction in the Eastern California shear zone, *Geology*, *29*(11), 975–978, doi:10.1130/0091-7613(2001)029<0975:TSAAFI>2.0.CO;2.

Rohatgi, V. K. (1976), *An Introduction to Probability Theory and Mathematical Statistics*, John Wiley, New York.

Ryerson, F. J., P. Tapponnier, R. C. Finkel, A.-S. Mériaux, J. Van Der Woerd, C. Lasserre, and M.-L. Chevalier (2006), Applications of morphochronology to the active tectonics of Tibet, *Spec. Pap. Geol. Soc. Am.*, *415*, 61–68.

Shen, Z. K., M. Wang, Y. X. Li, D. D. Jackson, A. Yin, D. N. Dong, and P. Fang (2001), Crustal deformation along the Altyn Tagh fault system, western China, from GPS, *J. Geophys. Res.*, *106*(B12), 30,607–30,621.

Stone, J. O. (2000), Air pressure and cosmogenic isotope production, *J. Geophys. Res.*, *105*(B10), 23,753–23,759, doi:10.1029/2000JB900181.

Tapponnier, P., and P. Molnar (1977), Active faulting and tectonics in China, *J. Geophys. Res.*, *82*(20), 2905–2930, doi:10.1029/JB082i020p02905.

Tapponnier, P., Z. Q. Xu, F. Roger, B. Meyer, N. Arnaud, G. Wittlinger, and J. S. Yang (2001), Oblique stepwise rise and growth of the Tibet plateau, *Science*, *294*(5547), 1671–1677, doi:10.1126/science.105978.

Taylor, J. R. (1997), *An Introduction to Error Analysis: The study of Uncertainties in Physical Measurements*, 2nd ed., Univ. Sci. Books, Sausalito, Calif.

Thatcher, W. (2007), Microplate model for the present-day deformation of Tibet, *J. Geophys. Res.*, *112*, B01401, doi:10.1029/2005JB004244.

Van der Woerd, J., F. J. Ryerson, P. Tapponnier, Y. Gaudemer, R. C. Finkel, A. S. Meriaux, M. W. Caffee, G. G. Zhao, and Z. Q. He (1998), Holocene left-slip rate determined by cosmogenic surface dating on the Xidatan segment of the Kunlun fault (Qinghai, China), *Geology*, *26*(8), 695–698, doi:10.1130/0091-7613(1998)026<0695:HLSRDB>2.3.CO;2.

Van der Woerd, J., F. J. Ryerson, P. Tapponnier, A. S. Meriaux, Y. Gaudemer, B. Meyer, R. C. Finkel, M. W. Caffee, G. G. Zhao, and Z. Q. Xu (2000), Uniform slip-rate along the Kunlun Fault: Implications for seismic behaviour and large-scale tectonics, *Geophys. Res. Lett.*, *27*(16), 2353–2356, doi:10.1029/1999GL011292.

Van der Woerd, J., X. W. Xu, H. B. Li, P. Tapponnier, B. Meyer, F. J. Ryerson, A. S. Meriaux, and Z. Q. Xu (2001), Rapid active thrusting along the northwestern range front of the Tanghe Nan Shan (western Gansu, China), *J. Geophys. Res.*, *106*(B12), 30,475–30,504, doi:10.1029/2001JB000583.

Van der Woerd, J., A. S. Mériaux, Y. Klinger, and P. Tapponnier (2002a), The November 14th, 2001, Mw = 7.8 Kokoxili earthquake in north Tibet (Qinghai province, China), *Seismol. Res. Lett.*, *73*, 125–135, doi:10.1785/gssrl.73.2.125.

Van der Woerd, J., P. Tapponnier, F. J. Ryerson, A. S. Meriaux, B. Meyer, Y. Gaudemer, R. C. Finkel, M. W. Caffee, G. G. Zhao, and Z. Q. Xu (2002b), Uniform postglacial slip-rate along the central 600 km of the Kunlun Fault (Tibet), from Al-26, Be-10, and C-14 dating of riser offsets, and climatic origin of the regional morphology, *Geophys. J. Int.*, *148*(3), 356–388, doi:10.1046/j.1365-246x.2002.01556.x.

Van der Woerd, J., Y. Klinger, K. Sieh, P. Tapponnier, F. J. Ryerson, and A. S. Mériaux (2006), Long-term slip rate of the southern San Andreas Fault from Be-10-Al-26 surface exposure dating of an offset alluvial fan, *J. Geophys. Res.*, *111*, B04407, doi:10.1029/2004JB003559.

Vergnolle, M., E. Calais, and L. Dong (2007), Dynamics of continental deformation in Asia, *J. Geophys. Res.*, *112*, B11403, doi:10.1029/2006JB004807.

Wallace, K., G. H. Yin, and R. Bilham (2004), Inescapable slow slip on the Altyn Tagh fault, *Geophys. Res. Lett.*, *31*, L09613, doi:10.1029/2004GL019724.

Wang, Q., et al. (2001), Present-day crustal deformation in China constrained by global positioning system measurements, *Science*, *294*(5542), 574–577, doi:10.1126/science.1063647.

Washburn, Z., J. R. Arrowsmith, S. L. Forman, E. Cowgill, X. F. Wang, Y. Q. Zhang, and Z. L. Chen (2001), Late Holocene earthquake history of the central Altyn Tagh fault, China, *Geology*, *29*(11), 1051–1054, doi:10.1130/0091-7613(2001)029<1051:LHEHOT>2.0.CO;2.

Washburn, Z., J. R. Arrowsmith, G. Dupont-Nivet, W. X. Feng, Z. Y. Qiao, and Z. L. Chen (2003), Paleoseismology of the Xorxol segment of the central Altyn Tagh Fault, Xinjiang, China, *Ann. Geophys.*, *46*(5), 1015–1034.

Wright, T. J., B. Parsons, P. C. England, and E. J. Fielding (2004), InSAR observations of low slip rates on the major faults of western Tibet, *Science*, *305*(5681), 236–239, doi:10.1126/science.1096388.

Zechar, J. D., and K. L. Frankel (2009), Incorporating and reporting uncertainties in fault slip rates, *J. Geophys. Res.*, *114*, B12407, doi:10.1029/2009JB006325.